Using multiple chronometers to establish a long, directly-dated lacustrine record

Roberts, Helen M.; Ramsey, Christopher Bronk; Chapot, Melissa S.; Deino, Alan L.; Lane, Christine S.; Vidal, Céline; Asrat, Asfawossen; Cohen, Andrew; Foerster, Verena; Lamb, Henry F.; Schäbitz, Frank; Trauth, Martin H.; Viehberg, Finn A.

Published in:
Quaternary Science Reviews

DOI:
10.1016/j.quascirev.2021.107025

Publication date:
2021

Roberts, H.M., Bronk Ramsey, C., Chapot, M.S., Deino, A.L., Lane, C.S., Vidal, C., Asrat, A., Cohen, A., Foerster, V., Lamb, H.F., Schäbitz, F., Trauth, M.H., Viehberg, F. (2021). Using multiple chronometers to establish a long, directy-dated lacustrine record: constraining >600,000 years of environmental change at Chew Bahir, Ethiopia. (Invited research article). Quaternary Science Reviews. DOI: 10.1016/j.quascirev.2021.107025

Using multiple chronometers to establish a long, directly-dated lacustrine record: constraining >600,000 years of environmental change at Chew Bahir, Ethiopia

Helen M. Roberts*[1], Christopher Bronk Ramsey[2], Melissa S. Chapot[1], Alan L. Deino[3], Christine S. Lane[4], Céline Vidal[4], Asfawossen Asrat[5,6], Andrew Cohen[7], Verena Foerster[8], Henry F. Lamb[1,9], Frank Schäbitz[8], Martin H. Trauth[10], Finn A. Viehberg[11]

1. Department of Geography and Earth Sciences, Aberystwyth University, Aberystwyth, SY23 3DB, UK.
2. School of Archaeology, University of Oxford, 1 South Parks Road, Oxford, OX1 3TG, UK
3. Berkeley Geochronology Center, 2455 Ridge Road, Berkeley, CA 94709, USA
4. Department of Geography, University of Cambridge, Cambridge, CB2 3EN, UK
5. School of Earth Sciences, Addis Ababa University, P.O. Box 1176, Addis Ababa, Ethiopia
6. Department of Mining and Geological Engineering, Botswana International University of Science and Technology, Private Bag 16, Palapye, Botswana
7. Department of Geosciences, University of Arizona, Tucson, AZ 85721 USA
8. Institute of Geography Education, University of Cologne, Gronewaldstraße 2, 50931, Köln, Germany
9. Botany Department, School of Natural Sciences, Trinity College Dublin, Ireland.
10. Institute of Geosciences, University of Potsdam, Karl-Liebknecht-Str. 24-25, 14476 Potsdam, Germany
11. Institute for Geography and Geology, University of Greifswald, Friedrich-Ludwig-Jahn Straße 16, 17489 Greifswald, Germany

*Corresponding author: hmr@aber.ac.uk

Science Highlights

- Four independent dating methods applied to ~293 m lake core from southern Ethiopia
- Reveals 620 ka high-resolution sedimentary record near key fossil hominin sites
- Mean accumulation rate of 0.47 mm/a comparable to other African lacustrine sediments
- Accumulation rate fell to 0.1 mm/a during MIS 2, likely due to reduced sediment supply
- Use of multiple independent chronometers is a powerful approach in lake settings

Keywords: Geochronology; optically stimulated luminescence; OSL; quartz; radiocarbon; $^{40}Ar/^{39}Ar$ dating; SCTF; tephrochronology; Quaternary; Ethiopia

Abstract

Despite eastern Africa being a key location in the emergence of *Homo sapiens* and their subsequent dispersal out of Africa, there is a paucity of long, well-dated climate records in the region to contextualize this history. To address this issue, we dated a ~293 m long composite sediment core from Chew Bahir, south Ethiopia, using three independent chronometers (radiocarbon, $^{40}Ar/^{39}Ar$, and optically stimulated luminescence) combined with geochemical correlation to a known-age tephra. The site is located in a climatically sensitive region, and is close to Omo Kibish, the earliest documented *Homo sapiens* fossil site in eastern Africa, and to the proposed dispersal routes for *H. sapiens* out of Africa. The 30 ages generated by the various techniques are internally consistent, stratigraphically coherent, and span the full range of the core depth. A Bayesian age-depth model developed using these ages results in a chronology that forms one of the longest independently dated, high-resolution lacustrine sediment records from eastern Africa. The chronology illustrates that any record of environmental change preserved in the composite sediment core from Chew Bahir would span the entire timescale of modern human evolution and dispersal, encompassing the time period of the transition from Acheulean to Middle Stone Age (MSA), and subsequently to Later Stone Age (LSA) technology, making the core well-placed to address questions regarding environmental change and hominin evolutionary adaptation. The benefits to such studies of direct dating and the use of multiple independent chronometers are discussed.

1. Introduction

The impact of climate and environmental change on hominin evolution, adaptation and dispersal in Africa has been the subject of much debate in recent years. Some of the dramatic events of the last half-million years include megadroughts (e.g. Scholz et al., 2007), faunal change and extinctions, the emergence of *Homo sapiens* (e.g. Hublin et al., 2017; McDougall et al., 2008; Brown et al., 2012; Potts et al., 2018), major transitions in tool technologies (e.g. MSA and LSA; Morgan and Renne, 2008; Gliganic et al., 2012; Brooks et al., 2018; Deino et al., 2018), and the dispersal of our species out of Africa (e.g. Soares et al., 2012; Groucutt et al., 2015; Stringer and Galway-Witham, 2018). However, despite all of these having been documented in eastern Africa, there is a relative paucity of long, well-dated, continental climate records in the region, which precludes robust correlations to local climate and environmental factors.

Lacustrine sediments in eastern Africa potentially offer some of the longest and finely resolvable terrestrial records of climate and environmental change (e.g. Cohen et al., 2016). A critical component of the work to understand these records lies in establishing the timing and rate of such change. Direct dating of sediments containing proxy records of palaeoclimate avoids the potential circularity of orbital tuning of one palaeoclimate record to provide a chronologic framework to apply to other records. However, direct dating of long sedimentary sequences can be challenging. The classic approach to dating sediments from lacustrine environments is to use radiocarbon techniques (e.g. Burnett et al., 2011; Roberts et al., 2018). This has been the mainstay of much work involving direct dating of lake sediments, but the relatively young upper age limit of ~45 ka, and limited availability of suitable sample material, means that for longer sedimentary records other dating strategies must also be used in concert with radiocarbon dating. For example, luminescence dating can be applied to minerogenic sediments throughout sediment cores over timescales spanning hundreds of thousands of years (e.g. Roberts et al., 2018), whilst ^{40}Ar/^{39}Ar dating is a more opportunistic technique due to the reliance on the presence of suitable minerals within tuffaceous zones but can be applied over an even greater time range encompassing the whole of hominin evolution (e.g. Deino et al., 2018). Indirect numerical dating can also be applied to long sedimentary records where opportunities arise to establish a correlation between a unit within a sediment core to one that has been directly dated at another locality, such as a tephra unit present in both a core and an outcrop (e.g. Lane et al., 2013). Palaeomagnetic reversals and geomagnetic excursions reflecting past changes in the Earth's geomagnetic field have also been used where records are sufficiently long and distinct (e.g. Sier et al., 2017).

All dating methods have their complications and assumptions, some of which are more acute within lacustrine settings. For example, depending upon the geology of the catchment and the chemistry of the lake, there can be concerns about potential reservoir effects on radiocarbon dates. Similarly, questions arise regarding the efficacy of bleaching of luminescence signals and dose rate for luminescence dating. And there are issues regarding presence and preservation of appropriate minerals for ^{40}Ar/^{39}Ar dating, or of distinctive stratigraphic units for correlation from core to outcrop. However, when combined, the use of such multiple, independent, direct dating techniques can be a powerful and compelling means of developing a chronology for long sedimentary records. Here we demonstrate this approach using three independent, direct dating methods (the radiometric techniques radiocarbon, optically stimulated luminescence, and ^{40}Ar/^{39}Ar), and tephrochronology where a correlation is made to a radiometric age determined in outcrop. This paper focuses upon the development of a chronology based on direct dating of sediments retrieved from the Chew Bahir basin, thereby creating a record with the potential to advance understanding of the palaeoclimatic context of hominin evolution and dispersal of *H. sapiens* from eastern Africa (Foerster et al., 2012, 2015, 2018; Schäbitz et al., in review; Trauth et al., 2021; Viehberg et al., 2018) free from the circularities inherent in the use of orbital tuning (e.g. Duesing et al., 2021), and benefitting from the use of multiple independent chronometers.

2. Study Area

The study site, Chew Bahir, is a playa lake located in southern Ethiopia (Fig. 1), approximately 70 by 30 km across. It is situated within a tectonic basin in the southern part of the Main Ethiopian Rift (MER), at an elevation of around 500 m above sea level, bounded to the west by the Hammar range and to the east by the Teltele-Konso range (Foerster et al., 2012). The total sediment depth in the basin exceeds 5 km, according to unpublished airborne gravity and seismic reflection data, offering potential records of climate and environmental change that probably span several million years. Chew Bahir is located within a climatically-sensitive region, influenced by multiple air-masses and wind systems, affecting the position and intensity of the tropical rain belt, the Congo Air Boundary (CAB), and the Indian Ocean Monsoon, coupled with regional influences associated with orography and the presence of large lakes (Nicholson, 2017). The present-day lake basin experiences annual wetting and drying cycles, with two wet periods, typically October to November and March to May (Nicholson, 2017). Lake levels in the past could have been up to ~45 m higher, as indicated by the height of the overflow level relative to the present-day basin floor (Foerster et al., 2012; Fischer et al., 2020). When lake levels were sufficiently high, palaeo-lake Chew Bahir overflowed into Lake Turkana, the last of the chain of lakes fed by the Abaya-Chamo lake system of the East African Rift System (Junginger and Trauth, 2013), and a lake could have persisted at Chew Bahir for extended periods of time with increased precipitation (Fischer et al., 2020).

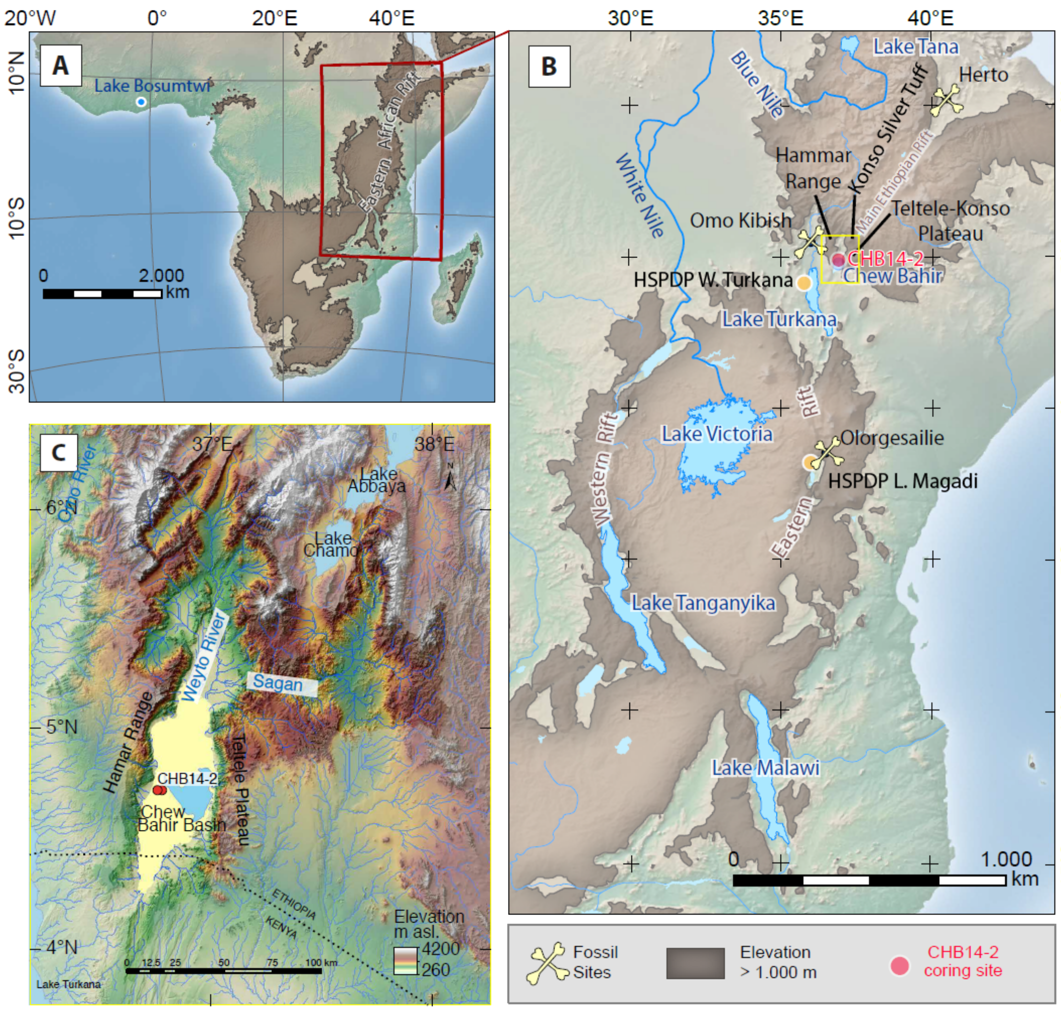

Figure 1a-c: Location of Paleolake Chew Bahir, southern Ethiopia, showing rift systems and highland areas in excess of 1000 m elevation. Also shown are major lakes, three of five Hominin Sites And Paleolakes Drilling Project (HSPDP) lacustrine core sites, and some of the earliest *Homo sapiens* sites in eastern Africa (Herto, Omo Kibish).

The closed-basin morphology of Chew Bahir and its climatically-sensitive location make it an ideal site from which to obtain records of past climate and environmental change. Additionally, the Chew Bahir site is located only ~90 km from Omo Kibish, at 195 ± 5 ka (McDougall et al., 2005) the site of the earliest known *Homo sapiens* fossils in eastern Africa (Fig. 1). The archaeological record of the region surrounding Chew Bahir also spans five key cultural transitions, including the transition from Mode 2 to Mode 3 technologies (c. 300-250 ka), the appearance of composite tools (c. 300 ka), the abandonment of bifaces (c. 200-160 ka), the appearance of blade industries (sporadically prior to and consistently after c.100 ka), and the emergence of regional stone point traditions (after c.250 ka). The site also lies close to proposed dispersal routes for *Homo sapiens* out of Africa. Chew Bahir is therefore a potentially significant site for the study of the palaeoclimatic context of human evolution and dispersal. However, the proxy records preserved in the sediments of the lake basin are of limited value without a reliable chronology.

3. Overview of the Chew Bahir drill cores and their composite stratigraphy

Two deep-drill cores were taken from the western margin of the Chew Bahir basin during November to December 2014, as part of the Hominin Sites and Paleolakes Drilling Project (HSPDP). Duplicate drill-cores HSPDP-CHB14-2A and HSPDP-CHB14-2B (hereafter referred to as cores 2A and 2B) were retrieved from vertical boreholes located ~20 m apart. Core 2A extended to 278.58 m below the sediment surface (mbs), whilst core 2B extended to 266.38 mbs (Cohen et al., 2016; Campisano et al., 2017, Foerster et al., submitted). Recovery for both cores exceeded 85%, and cores 2A and 2B each comprised more than 115 core sections.

All ~545 m of the core sections for cores 2A and 2B were split lengthwise, their lithology described, photographed to produce high resolution line-scan images, logged using Multi-Sensor Core Loggers (MSCL, XYZ point sensor data), and finally subsampled at the National Lacustrine Core Facility (LacCore) at the University of Minnesota following HSPDP protocols (Campisano et al., 2017). These initial datasets, and other datasets acquired or refined later, were used to correlate key features between duplicate cores 2A and 2B, enabling the development of a single continuous composite profile of 292.87 m total length (where depth down-core is described in metres composite depth, mcd) based on 'spliced' core sections from both core 2A and 2B (Fig. 2) (Foerster et al., submitted). This multi-parameter approach used visual characteristics, sedimentological data, line scan images, and magnetic susceptibility (MS; both loop sensor and high-resolution point MS) data sets to establish inter-core correlations. Subsequently, high-resolution scanning µXRF data sets were used for final small-scale refinements of the correlations and to inform the development of the composite core used in the present paper. Version 3.0 of the core-to-core correlation provides spliced and largely continuous high resolution µXRF and multi-sensor core logging data sets along the composite core equivalent to a recovery in excess of 90%.

The Chew Bahir cores 2A and 2B (Fig. 2) are mostly comprised of fine green-greyish to light coloured, reddish and brown silty and sandy clays intercalated by few mica-rich, partly mm-scale laminated silt and sand beds, some of them calcareous (Cohen et al., 2016; Campisano et al., 2017; Foerster et al., submitted). Shell-rich horizons occur throughout the core. Below 90 m composite depth (mcd), occurrences of nodules and large carbonate-rich concretions increase. No clearly developed palaeosols are visible in the core, although there may be some potential palaeosol development in the deepest part of the core, as described for HSPDP Magadi and Turkana sites (Cohen et al., 2016; Owen et al., 2018), suggesting post-depositional early diagenetic processes that have also been previously identified in a 40 m core from the centre of the Chew Bahir basin (Viehberg et al., 2018).

Subsamples of the core material were typically taken from the composite core at ~32 cm resolution, although higher resolution increments as little as 0.5 cm were used for selected intervals to generate more material-specific proxy datasets. Palynological investigations demonstrated that fossil pollen and spores are not preserved in countable amounts in the deposits; this is probably due to exposure to oxygen during intermittent desiccation of the exposed sediment surface. Diatoms and ostracods were preserved in only a few distinct layers in the core sediments, including regions where tephra glass shards were also preserved; the chemistry of the palaeolake water may have compromised their preservation beyond these few units. Overall, ~14,000 discrete sediment samples were taken from the Chew Bahir cores. This total included opportunistic samples taken where appropriate materials were noted, such as those for the analysis of biomarkers, and also for direct dating. Many more samples were taken to explore the potential for dating, or to inform the methods used, than ultimately gave rise to numerical ages (discussed in section 4 below, for each technique). Figure 2 shows the down-core locations of the 30 samples that generated the ages considered in this paper.

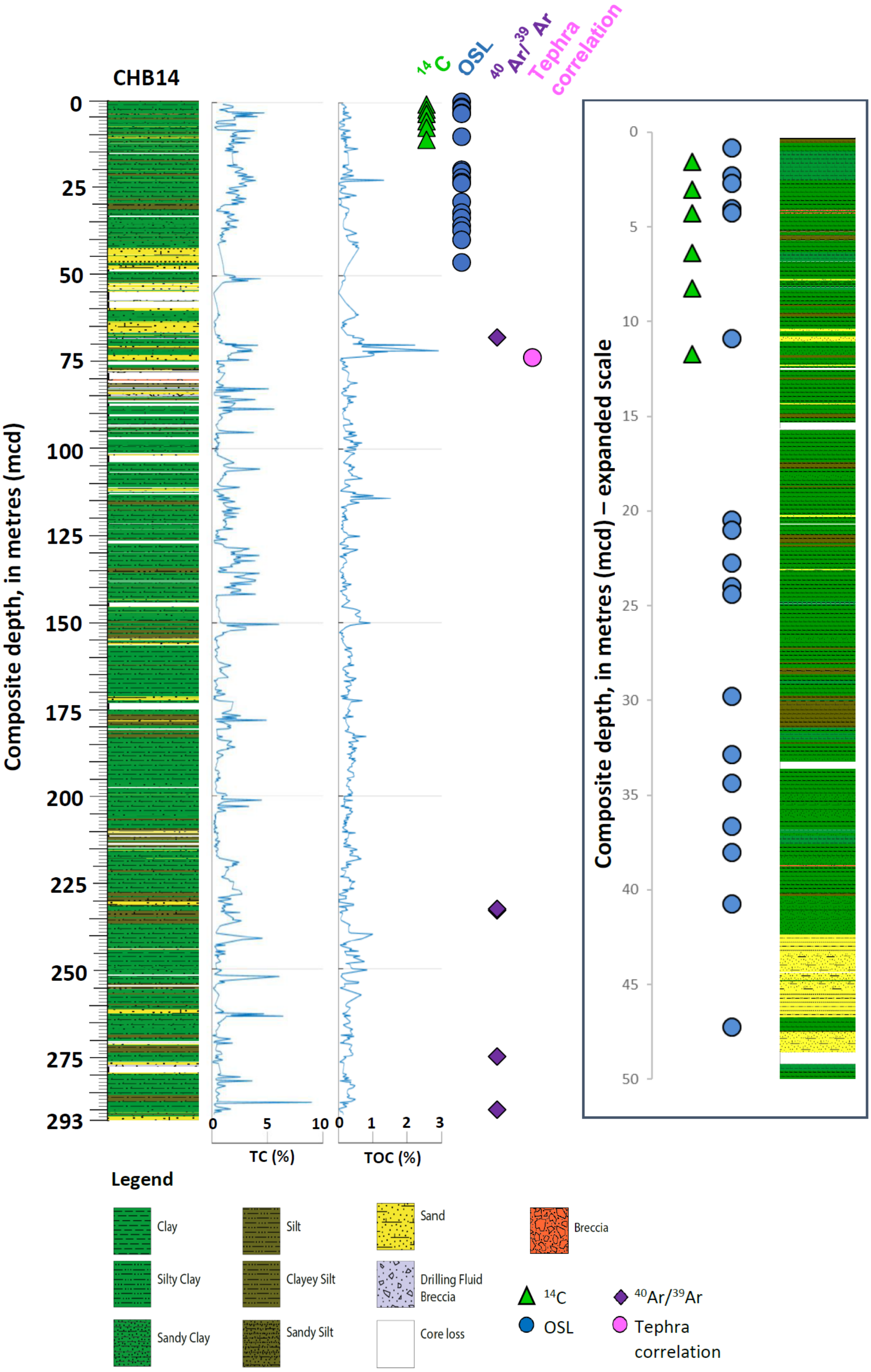

Figure 2: Overview of the stratigraphy of the ~293 m composite core (HSPDP-CHB14) from Chew Bahir, which is chiefly comprised of fine unconsolidated clays and silty clays (shown as green in colour) with some sands (depicted in yellow). Total carbon (TC %) and total organic carbon (TOC %) are given. Also shown are the depths from which the various

samples used for age-depth modelling were taken: six AMS radiocarbon dates from the upper 12 m, eighteen quartz OSL ages in the upper 50 m, five single crystal total fusion $^{40}Ar/^{39}Ar$ dates (two at ~240 mcd which overlap in this figure), and one correlated tephra sample. For clarity, the samples and stratigraphy from the upper 50 m of the composite core are also displayed on an expanded scale to the right of the diagram.

4. Age determinations using direct dating

To generate a chronology for the 293 m composite Chew Bahir core based on direct dating, several geochronologic techniques were used, namely radiocarbon, optically stimulated luminescence (OSL), $^{40}Ar/^{39}Ar$, and tephrochronology. The use of such multiple, independent chronometers, which rely on different materials for dating, offers the opportunity to cross-corroborate the ages generated and can give additional confidence to the chronology developed for the core sediments as a whole. The four techniques, and the ages generated are considered below, in sections 4.1-4.4.

4.1 **Radiocarbon Dating**

Radiocarbon dating of the composite core synthesised from cores HSPDP-CHB14-2A and -2B was not straightforward. The total carbon (TC) content of the core was typically low as illustrated in Fig. 2 (mean and standard deviation TC = 1.20 ± 1.04 %; mean and standard deviation for total organic carbon (TOC) = 0.30 ± 0.23 %; n=751), and no preserved plant macrofossils suitable for dating were found within the relevant depth range towards the upper portion of the core. A number of different approaches were therefore taken to try to overcome these issues, including the dating of pollen and microcharcoal concentrates, fish bones, and ostracods.

4.1.1 *Pollen concentrate*

At two positions within the composite core attempts were made to recover sufficient pollen to radiocarbon date by using pollen concentration. The samples underwent a sodium polytungstate density separation, but this yielded a mixture of organic remains including some pollen but also other components. The separated fractions were then freeze-dried, combusted and converted to graphite (Dee and Bronk Ramsey, 2000), and then AMS dated (Bronk Ramsey et al., 2004). One of these samples provided a date as shown in Table 1, but the other (from 2B-10H-1, 90-92cm) failed to produce sufficient carbon for dating. The single date obtained (OxA-X-2701-16, shown in Table 1) was, however, not considered reliable because of the very low carbon content (3.3%) following the extraction procedure. Given the poor preservation of pollen and the typically low carbon percentage within these HSPDP-CHB14-2A and -2B cores, radiocarbon dating of pollen concentrate was not pursued further.

4.1.2 *Fish bones*

Occurrences of fish bones were identified during initial core description from multiple levels within the HSPDP-CHB14-2A and -2B cores, and hand-picked from the core sections (2A-3H-1, 97-98 cm; 2A-8E-3, 102-103.5 cm; 2B-4H-2, 16-18 cm; 2B-4H-1, 147-149 cm; 2B-7H-2, 103.5-104 cm; 2B-7H-2, 105-107 cm). Attempts were made to date these by extraction of collagen, initially without ultrafiltration (Brock et al., 2010). However, in all cases there was no collagen recovered and it was concluded that the organic preservation of the bone was too poor. This is not surprising given the environmental conditions on the site and the relatively poor preservation of other biological proxies within the core material.

4.1.3 *Microscopic charcoal*

A test sediment sample from 74-76 cm depth within core section HSPDP-CHB14-2A-11E-1 underwent density separation using sodium polytungstate to extract the sub-mm sized charcoal, but it was impossible to pick these fragments manually and so the organic residues were extracted from bulk sediment. The sample was sieved at 20 µm to assess the organic content. A significant volume of sub-mm charcoal was present along with some insect chitin. This mixture was then freeze-dried, combusted and converted to graphite (Dee and Bronk Ramsey 2000), and then AMS dated (Bronk Ramsey et al. 2004), yielding a date of 26,400 ± 310 yr BP (OxA-X-2705-25; Table 2). The carbon content of the material was low (15.2%), and given the mixed nature of the material this was not considered to be a reliable method, especially as it was not possible to recover even these quantities from other sections where charcoal concentrations were thought to be high. No further analysis of microscopic charcoal was therefore attempted.

4.1.4 *Ostracods*

The radiocarbon method which worked best for this core was the dating of ostracod carapaces, which were available from a number of different levels within the core. A total of sixteen samples was assessed, and of these nine contained sufficient material for radiocarbon dating and the remaining seven were attempted, but were too small to process. Each sample underwent a standard acid digestion treatment for carbonates (Brock et al. 2010), and was then converted to graphite (Dee and Bronk Ramsey 2000) and AMS dated (Bronk Ramsey et al. 2004). The results from these measurements are shown in Table 3.

Two of the samples (Nos. 77 and 118) yielded very low levels of carbon (<100 µg C; Table 3) and were thought to be unreliable for this reason, given the risk of other geological carbonates or of exchange. These two samples are both given OxA-X numbers in Table 3 (OxA-X-2731-50 and OxA-X-2731-53), but are not used in the subsequent age-depth model. Any radiocarbon samples are potentially susceptible to contamination from a number of sources so it is important to correct for this with background material. In this study, a background reference ostracod sample was taken from a depth of 74.435 m, which should contain no radiocarbon. The date obtained for this is 38,840 ± 390 BP (Table 3), which corresponds to about 0.8% modern. This is relatively high for a carbonate background sample, but presumably best reflects the nature of these particular samples in this context. All dates were therefore corrected on the basis of this measurement, using a conservative approach with the uncertainty in the correction taken to be equal in size to the correction itself. The corrected radiocarbon dates are given in Table 3 and used in the age-depth modelling discussed later. One of the dates (Sample No. 96, OxA-35657) after correction is very close to background and would normally be reported as greater than 28,200 BP, but here the measurement has been used in the age-depth model because it does still provide useful information. Note that the discounted date for sample 118 (Table 3) is also very close to background after correction.

In total, six viable corrected radiocarbon ages (BP) were derived from dating of ostracods (indicated in Table 3 by *). These ages are in chronostratigraphic order and extend through the upper ~12 m of the ~293 m composite core, covering the last ~40,000 years of the sedimentary record at Chew Bahir. To account for the fact that the ostracods live within the lake and therefore the ages of their shells are possibly too high due to calcification in water with a reservoir age of up to 3,000 years (e.g. Junginger et al., 2014), allowance was made for a dead carbon fraction in the age-depth model (discussed in section 5, below).

4.2 **Luminescence Dating**

Luminescence dating has made some major breakthroughs in both accuracy and precision in recent years, and the dating techniques and applications are still evolving. Today, a family of luminescence signals suitable for sediment dating exist, and these can now make a contribution to the dating of lake sediments (Roberts et al., 2018). One of the advantages that luminescence dating brings to the study of lacustrine sediments is that the commonly occurring minerals quartz and feldspar are used, and given their abundance, luminescence dating can typically be applied throughout sediment cores, rather than relying on opportunistic sampling such as for tephra or for materials suitable for radiocarbon dating. Additionally, when applied to sediments, these luminescence techniques date the deposition event directly, recording the last exposure of the sediments to daylight prior to burial by further accumulating sediments. These luminescence dating techniques also span a useful time range which typically extends from tens of years to several hundred thousand years.

4.2.1 *Materials and methods for luminescence dating*

A total of 82 samples was taken from the full range of depths across cores HSPDP-CHB14-2A and -2B to support the luminescence dating work of the ~293 m composite core from Chew Bahir. The frequency of sampling varied through the composite core, with sampling becoming less frequent with increased depth in the cores, to reflect: a) the anticipated reduction in absolute precision with the increase in age (i.e. when % uncertainty on an age is expressed in ka); and b) considering the likely depths in the core where onset of saturation of the luminescence signal might be anticipated based on other 'typical' accumulation rates for other lake cores, including other work at Chew Bahir using much shorter cores taken close to the centre of the basin (e.g. Viehberg et al., 2018). Luminescence samples were taken from the 'working half' of the half-round core lengths after the cores had been split and the sediments described in white light. The luminescence samples were taken in subdued red-lighting conditions, avoiding sampling near any cracks in the sediment, and taking care to remove the outer light-exposed portions of the core and reserve these for assessment of the dose rate. The materials sampled ranged from dominantly sand-sized sediments to fine-grain units containing silts and clays.

Material of fine-silt size (4-11 µm diameter) was available throughout the core, and was separated for luminescence investigations of all 82 samples by treatment of the bulk, non light-exposed sediments using a 10% v/v dilution of hydrochloric acid to remove carbonates, followed by 20 vol hydrogen peroxide to remove organics, then Stokes Law settling using 0.01N sodium oxalate to isolate grains of 4-11 µm diameter. The resultant 'polymineral' (mixed mineralogy) fine-grain material was deposited onto aluminium discs of 9.7 mm diameter by settling in acetone, using 1 mg of 4-11 µm diameter material per disc (termed an 'aliquot'). Although such mixed-mineralogy fine-grain material can be used for luminescence dating (e.g. Roberts et al., 2018) thanks to advances in measurement protocols (see reviews by Buylaert et al., 2012; Li et al., 2014), where possible quartz remains the mineral of choice for luminescence dating due the stability of the quartz optically stimulated luminescence (OSL) signal over time, and because this is the luminescence signal that is removed ('bleached') most rapidly in nature during transport and deposition (Roberts, 2008). All 82 samples were screened for the likely presence of quartz by examining the thermoluminescence (TL) signal from polymineral fine-grain aliquots in response to a given radiation dose, viewed through U-340 filters, to check for the presence of a characteristic TL peak from quartz visible at ~110 °C when heating at a rate of 5°C/s. Where this 110 °C TL peak was visible, chemical treatment of the 4-11 µm diameter polymineral material using concentrated hydrofluorosilicic acid (H_2SiF_6) for 14 days was used to selectively dissolve feldspars and isolate quartz grains (Roberts, 2007). Following these screening and preparation procedures, 34 of the 82 samples contained sufficient 4-11 µm diameter quartz to proceed to further investigations for luminescence dating.

Luminescence measurements were made using an automated Risø TL/OSL-DA-20 laboratory instrument equipped with a Sr/Y beta irradiation source delivering ~0.077 Gy/s. Optical stimulation of fine-grained quartz was achieved using blue (470 Δ 20nm) light emitting diodes (LED), and detection was through 7.5mm thickness of Hoya U-340 glass filter. Luminescence dating and characterisation measurements were made using a Single-Aliquot Regenerative dose (SAR) measurement protocol applied to fine-grained quartz. All thermal pretreatments were recorded as TL.

The light-exposed parts of the samples used for dating were gently dried, milled to a fine powder, and used to assess the dose rate to the samples, via thick-source alpha-counting using Daybreak™ alpha counters and beta-counting using a Risø GM-25-5™ beta counter. To simplify the assessment of the dose rate, luminescence samples were typically taken away from major changes in the core stratigraphy; where this was not possible, ancillary dose rate samples were taken from neighbouring stratigraphic units observed within ± 30 cm depth from the luminescence dating sample location. The cosmic dose rate contribution was assessed according to Prescott and Hutton (1988, 1994), and assuming a typical lake water depth over time of 10 m after consideration of former shorelines and the overflow depth of 45 m above the basin floor (Fisher et al., 2020). Water content measurements were made on the sediments sampled for luminescence dating, expressed as mass water/mass dry sediment. These values compared favourably to the more continuous record obtained as part of higher-resolution loss on ignition (LOI) work which involves an initial step of heating to 105°C, and given the high percentage core recovery on drilling (section 3), the water content values measured for the luminescence samples ± 10% were used for calculation of the dose rate to those samples. These values and the total dose rates to the samples used for dating are shown in Table 4.

4.2.2 *Assessment of equivalent dose for luminescence dating*

Measurements to assess the equivalent dose (D_e, in Gy) were made using a single aliquot regenerative dose (SAR) technique applied to fine-grained quartz. The conditions for dating measurements were selected following preheat tests and preheat dose recovery tests conducted at a variety of temperatures for three of the 34 samples for which fine-grained quartz was recovered. A preheat of 240°C for 10 s was applied prior to measurement of the natural (L_N) or regenerative dose (L_X) signal, and the preheat used prior to measurement of the test dose signal (T_N or T_X) was 200°C for 10s. The signal was taken from the first 0.8 s of a 50 s stimulation with blue diodes, and the background from the final 10 s. Aliquots examined for dating tended to perform well, typically passing a number of quality control criteria used to screen the data including having recycling ratios within 1.0 ± 0.1, recuperation of signal of < 5%, and assessments of signal intensity. An OSL IR depletion ratio test (Duller, 2003) was used to assess the purity of the fine-grained separate that had been prepared as quartz. From the total of 34 samples prepared, an initial suite of 17 samples for which there was a relatively large amount of material was tested. Of these, 14 samples had OSL IR depletion ratios outside the 1.0 ± 0.1 screening threshold indicating the presence of IR-responsive material contributing to the blue OSL signal, suggesting feldspar grains may also be present in these quartz separates. For the remaining samples prepared as quartz, there was much less material recovered (often fewer than 20 aliquots), and for this reason as a precautionary measure a post-IR OSL (Banerjee et al., 2001) measurement protocol was used for dating these remaining samples, as well as for the 14/17 larger samples described above. This measurement protocol uses stimulation with infra-red (IR) light to remove the signal from feldspar, leaving a blue OSL-responsive signal dominated by quartz that is used for dating. Whilst 31 of the 34 samples prepared as fine-grained quartz used the post-IR OSL signal for dating as a precautionary measure, the OSL IR depletion ratio examined at the end of these dating measurement cycles indicated that only 12 of the 34 samples had values that were beyond the 1.0 ± 0.1 range, suggesting that most of the samples prepared as quartz were dominated by quartz in any case.

4.2.3 *Defining the upper limit of saturation of equivalent dose*

The maximum age of the sediments in the Chew Bahir core was anticipated to extend significantly beyond the upper limit of dating using quartz OSL. Defining this upper limit of OSL dating is important because working at or beyond the saturation limit in nature can lead to age underestimates. However, in practice defining this upper limit of reliability can be difficult, because it varies according to the specific luminescence signal used, the dose rate, and due to variability between individual samples. Additionally, work by Chapot et al. (2012) based on a known-age site (Luochuan, China) demonstrated that for older samples that had accumulated equivalent dose (D_e) values in excess of 150 Gy, finite ages showing age progression down-section could still be generated but the luminescence behaviour in the laboratory differed from the behaviour in nature, giving age underestimations for samples beyond 150 Gy. The limit of reliability of OSL ages in the work of Chapot et al. (2012) was demonstrated to be the point at which the response to increasing radiation doses delivered in the laboratory during measurements for dating (the 'dose response curve') deviated from the response to similar radiation doses delivered in the natural environment over much longer timescales (the 'natural dose response curve').

Building on the concept of the natural dose response curve (Chapot et al., 2012) and normalising for test doses (T_D, Gy) of different size (Roberts and Duller, 2004), natural OSL signals $(L_n/T_n)*T_D$ from all 34 Chew Bahir fine-grain quartz samples down core were used to explore the natural limit of saturation. In a natural dose response curve, L_n/T_n signals are plotted against expected dose (expected age * dose rate). Although there are no expected (i.e. 'known') ages in this study, the level of saturation for the Chew Bahir composite core can still potentially be explored by plotting $(L_n/T_n)*T_D$ against (depth * dose rate) (Fig. 3); incorporating T_D into the dataset plotted on the y-axis can account for measurements made using different instruments (Roberts and Duller, 2004), and incorporating dose rate into the x-axis dataset can help account for variations in dose rate between lithologically distinct units within the core. These data can be used in two different ways. Firstly and most straightforwardly, the $(L_n/T_n)*T_D$ values for the deepest part of the core that is unambiguously in saturation as far as the quartz OSL signal is concerned can be used to define a pragmatic upper limit for the likely reliability of dating, based on calculating 86% of the saturation level determined from the mean $(L_n/T_n)*T_D$ values for the deepest samples (Fig. 3). However, when the full dataset is examined it is found to be extremely coherent, showing a rapid initial increase in the $(L_n/T_n)*T_D$ values observed as (depth*dose rate) increases, followed by a slowing and then flattening to a consistent $(L_n/T_n)*T_D$ value of ~90 Gy at depth*dose rate values greater than ~200 Gy*m/ka. This natural signal dataset can be fitted with a single saturating exponential (Fig. 3), which suggests that the sediment accumulation rate is essentially constant over time (i.e. age is proportional to depth) for at least the upper third of the core where the signals show some progression (i.e. before the full impact of saturation occurs). This finding is interesting in its own right and has implications for the expected output from any age-depth model developed, but it also leads to a second potential means of determining a practical upper working limit for the onset of saturation for these samples of 'unknown' age based on the value of $2D_0$ when the whole 'pseudo natural dose response curve' dataset shown in Fig. 3 is fitted.

Both methods of exploring saturation of the quartz OSL signal give similar outcomes (Fig. 3), and suggest that the upper limit of reliability for the fine-grain quartz OSL samples at Chew Bahir is a value that equates to a radiation dose of ~150 Gy, the same limit noted by Chapot et al. (2012) for quartz from Chinese loess. Twenty three of the 34 natural OSL signals screened in this way were below the limit of saturation, shown in Fig. 3 as closed green circles. Using the natural signal or natural dose response curve to assess the limits of saturation avoids issues which may be caused if there is a mismatch between the response of the samples in laboratory versus natural settings (Chapot et al., 2012), although in this study matters are complicated by not having an independent assessment of age and hence the term 'pseudo natural dose response curve' is used to describe the data fitted in Figure 3. The coherence of these methods for assessing saturation gives confidence that a prudent upper limit for saturation has been defined for the fine-grained quartz OSL samples in this study, and the collection of samples that were clearly beyond the limit of saturation was key to defining this limit by both of the methods employed.

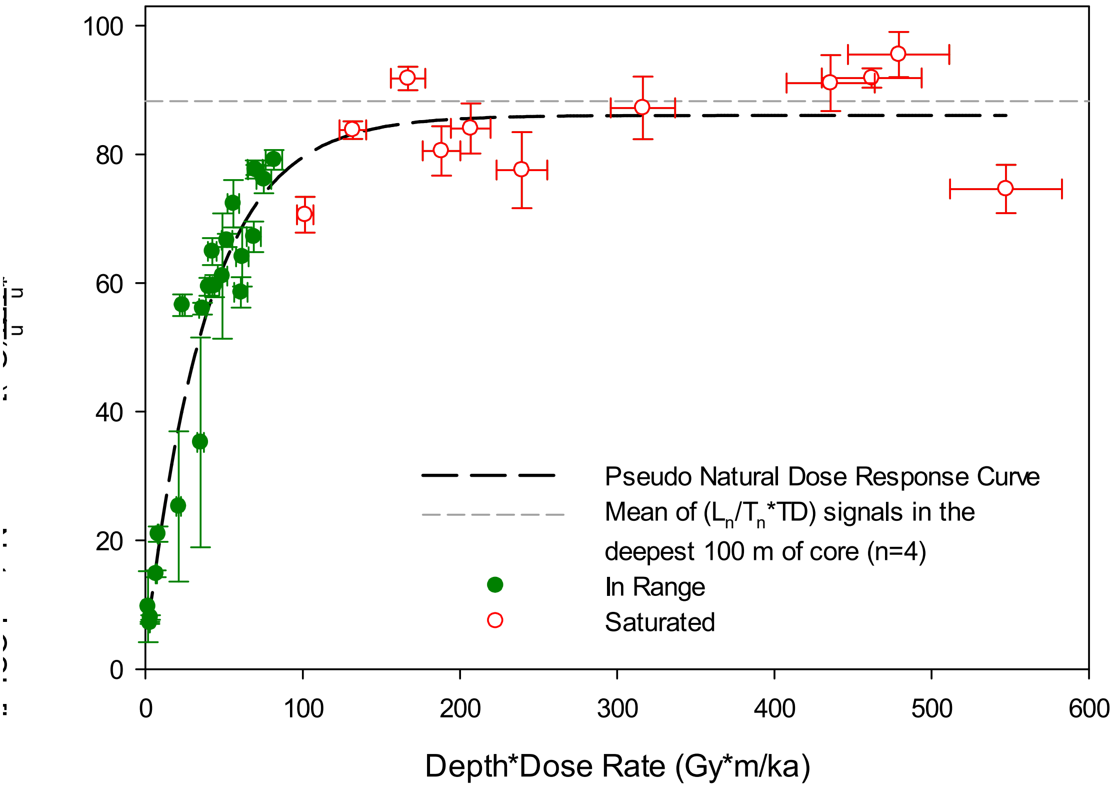

Figure 3: Two approaches to defining saturation of the quartz OSL signal in this study, based on the natural signal intensity. The simplest approach takes the mean of the normalised natural signal intensity (L_n/T_n * T_D) values of the deepest samples (mean value is shown in grey short dashed horizontal line, based on the 4 samples from the lowermost 100 m of the 293 m core which are effectively infinitely old as far as the OSL signal is concerned), and defines the limit of saturation as being 86% of that mean value. Also shown is the Pseudo Natural Dose Response Curve data created using the normalised natural signal multiplied by test dose (L_n/T_n * T_D) for all 34 quartz OSL samples, plotted against a proxy for the unknown absolute age based on composite depth in metres multiplied by dose rate to compensate for changes in lithological unit which may otherwise cause fluctuations in the L_n/T_n signal intensity. These data can be fitted with a single saturating exponential (long black dashed line) of the form: $I = I_0 + I_{max} * (1 - e^{-D/D_0})$, where I is the luminescence signal (here, L_n/T_n * T_D), D is related to the amount of radiation exposure (here defined as depth*dose rate), and D_0 is the characteristic dose at saturation. A value of 2*D_0 is viewed as a prudent upper limit for dating quartz (Wintle and Murray, 2006), and in practice essentially equates to 86% of L_n/T_n * T_D at saturation.

4.2.4 *OSL ages and comparison with radiocarbon ages*

A total of 34 fine-grain (4-11 µm diameter) quartz OSL samples were screened using the quality checks and screening criteria outlined in sections 4.2.1 to 4.2.3. Twenty three OSL samples were found to have a normalised natural signal below the limit of saturation, and of these a further five samples were rejected on the basis of low signal intensity, giving the 18 final quartz OSL ages shown in Table 4 and in the Bayesian age model of Figure 6.

The 18 OSL ages generated are in chronostratigraphic order, within errors, and span the uppermost ~50 m of the composite core. The quartz OSL ages are consistent with those from radiocarbon within uncertainties; however, the central values for the radiocarbon ages tend to be larger than those of the neighbouring luminescence ages. These two dating techniques are independent, and applied to different materials which relate to the age of different events. However, given that the radiocarbon ages are older than the luminescence ages, the suggestion is that the radiocarbon dates may be affected by a reservoir effect, the source of which may be from within the local catchment. Using Bayesian modelling techniques, a radiocarbon reservoir offset of ~1500 years is suggested (Supplementary Information Fig. S3), which is similar to the reservoir effect of 1900 years determined by Junginger et al. (2014) in a similar setting (Suguta Valley, northern Kenya rift). This offset is accounted for when the radiocarbon ages are subsequently combined with dates from other independent methods to develop an age-depth model for Chew Bahir (section 5).

Thus far, a combination of radiocarbon dates on ostracods (n=6) and fine-grain quartz OSL ages (n=18) have been used to constrain the ages of the upper ~50 m of sediment from the composite core. Beyond this depth, a different direct dating method is required to constrain the age of the ~293 m composite core as this extends beyond the maximum upper limit of both radiocarbon and quartz OSL dating.

4.3 Tephrochronometry: direct dating using the $^{40}Ar/^{39}Ar$ technique

The numerous volcanic sources within the Main Ethiopian Rift provide the potential to secure an extended chronology for the Chew Bahir record based on the application of $^{40}Ar/^{39}Ar$ dating of pyroclastic eruptions. Tuffaceous material is preserved within the Chew Bahir cores, deposited either as primary tephra fallout, or within fluvially derived sediments sampling the catchment following volcanic events. Using opportunistic sampling targeting tuffaceous zones, samples were taken for analysis using the $^{40}Ar/^{39}Ar$ dating technique applied to feldspars.

4.3.1 $^{40}Ar/^{39}Ar$ materials and methods

Tuffaceous zones in CHB14 were identified by visual examination of the high-resolution images for the composite core, with follow-up inspection of the working and archival core halves. In total, 23 samples were taken from the working core halves for further processing at the Berkeley Geochronology Center (BGC).

Mineral separation at BGC began with gentle disaggregation and wet sieving through a new 90-micron sieve bag. Feldspar in the coarser fraction was concentrated with a Frantz magnetic separator, hand-picked, washed in 5% HF and distilled water, and hand-picked again to obtain the clearest, most inclusion-free material.

The completed separates for $^{40}Ar/^{39}Ar$ dating were irradiated at the Oregon State University TRIGA reactor in three batches (BGC irradiation numbers 454 and 460 for 0.5 hours in the

CLICIT position, and 480 for 1.35 hours in the CLOCIT position, both positions Cd-lined). All irradiations employed sanidine from the Alder Creek Rhyolite of California (orbitally referenced age = 1.1848 ± 0.0006 Ma) (Niespolo et al., 2017) as the neutron-fluence monitor standard. Reactor-induced isotopic production ratios for the CLICIT were: $(^{36}Ar/^{37}Ar)_{Ca}$ = 2.65 ± 0.02 × 10^{-4}, $(^{38}Ar/^{37}Ar)_{Ca}$ = 1.96 ± 0.08 × 10^{-5}, $(^{39}Ar/^{37}Ar)_{Ca}$ = 6.95 ± 0.09 × 10^{-4}, $(^{37}Ar/^{39}Ar)_K$ = 2.24 ± 0.16 × 10^{-4}, $(^{38}Ar/^{39}Ar)_K$ = 1.220 ± 0.003 × 10^{-2}, $(^{40}Ar/^{39}Ar)_K$ = 2.5 ± 0.9 × 10^{-4}, and for the CLOCIT were $(^{36}Ar/^{37}Ar)_{Ca}$ = 2.649 ± 0.014 × 10^{-4}, $(^{38}Ar/^{37}Ar)_{Ca}$ = 3.33 ± 0.012 × 10^{-5}, $(^{39}Ar/^{37}Ar)_{Ca}$ = 9.1 ± 0.28 × 10^{-4}, $(^{38}Ar/^{39}Ar)_K$ = 1.208 ± 0.002 × 10^{-2}, $(^{40}Ar/^{39}Ar)_K$ = 4 ± 6 × 10^{-4}. Atmospheric $^{40}Ar/^{36}Ar$ = 298.56 ± 0.31 (Lee et al., 2006) and decay constants follow Min et al. (2000).

Following several weeks of radiological 'cooling' after irradiation, the feldspars were analyzed individually by the $^{40}Ar/^{39}Ar$ technique using single-crystal total-fusion (SCTF). In the SCTF technique, individual phenocrysts (here, feldspar) are heated rapidly to fusion in ultra-high vacuum using a partially focused CO_2 laser in a single step (although in some cases the grains are subjected to a very low power initial 'degas' step to drive off surficial argon). After a period of several minutes of gas cleanup to remove reactive species and H_2O, the purified Noble gas fraction was analyzed for argon isotopes on a Nu Instruments *Noblesse* noble-gas mass spectrometer, featuring a high-efficiency ionization source and simultaneous multi-isotope measurement using all ion-counting electron multiplier detection systems.

4.3.2 *$^{40}Ar/^{39}Ar$ age determinations*

Of the 23 samples taken for analysis from the Chew Bahir cores, a total of 12 samples (each comprising multiple age determinations on single feldspar grains) gave rise to useful $^{40}Ar/^{39}Ar$ age information, determined as outlined below and shown in Figure 4 and Table 5. These 12 can be further categorised into groups of adjacent or nearly adjacent core samples of the same eruptive event; these adjacent samples have been combined into five tuff units for statistical leverage. The remaining samples did not give useful ages due to a lack of datable phenocrysts (in the relatively young, fine-grained tuffaceous units encountered in the CHB core, successful single-crystal dating requires high-K phases such as sanidine), or to the presence of only anomalously old material. As is often the case in lacustrine tuffaceous units, age distributions obtained from a suite of SCTF analyses are complicated by anomalous results, from such sources as detrital contamination, excess ^{40}Ar trapped in primary phenocrysts, or subtle alteration. The steps taken to derive a primary eruption age from such distributions is described as follows:

First, analyses older than 1 Ma and younger than 0 Ma are omitted, considering that these are certainly xenocrysts (in the case of the older analyses) or either altered or not feldspars (in the case of the younger analyses). Secondly, older xenocrysts are excluded from the age population based on a procedure that evaluates age gaps in the ordered age distribution (described in Deino et al., 2019).

Finally, we note that many of the distributions are skewed toward older ages, and rather than use weighted means to calculate a representative eruption age, we employ a Bayesian estimation procedure (Keller et al., 2018; Deino et al., 2019). This procedure takes advantage of our ability to construct an informative prior estimate of the relative closure age distribution. Empirically, we observe that this distribution tends to take a roughly triangular

Roberts, H.M., Bronk Ramsey, C., Chapot, M.S., Deino, A.L., Lane, C.S., Vidal, C., Asrat, A., Cohen, A., Foerster, V., Lamb, H.F., Schäbitz, F., Trauth, M.H., Viehberg, F. (2021). Using multiple chronometers to establish a long, directy-dated lacustrine record: constraining >600,000 years of environmental change at Chew Bahir, Ethiopia. (Invited research article). Quaternary Science Reviews. DOI: 10.1016/j.quascirev.2021.107025

form, with a greater number of ages clustered around the youngest single age. A likelihood-based approach then allows us to estimate the depositional age and uncertainty for each sample.

The five SCTF $^{40}Ar/^{39}Ar$ ages generated (Table 5 and Fig. 4) are in stratigraphic order. They are chronostratigraphically consistent with the radiocarbon and OSL ages discussed previously, but extend far beyond the upper limit of these techniques to help constrain the full duration of the Chew Bahir record, indicating that the base of the composite core is in excess of 600,000 years old.

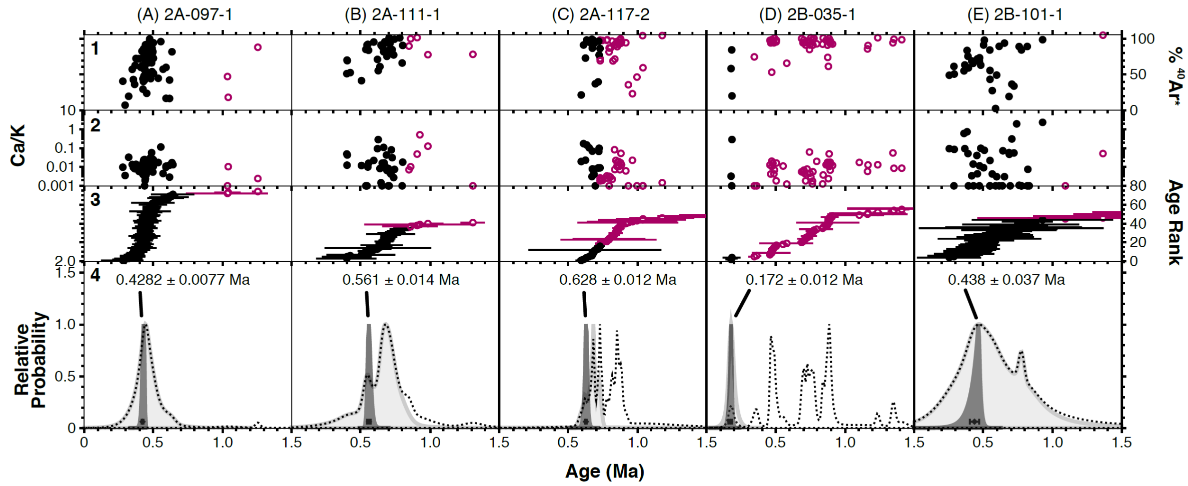

Figure 4: Age-probability density plots derived from the results of the $^{40}Ar/^{39}Ar$ dating experiments on individual feldspar phenocrysts. Five tuffaceous units are represented in plots A–E (see Table 5 for details of core intervals and composite depth down section). Panels 1–4 for each tuffaceous unit show 1) percent radiogenic ^{40}Ar of the extracted gas; 2) atomic Ca/K ratio; 3) the age rank and 1σ analytical error, and 4) the age-probability density spectra. Ages (with 1σ uncertainty) are posterior estimates derived from the Bayesian depositional age modelling described in section 4.3.2. The dashed line represents the age-probability density curve of all analyses for a given tuff unit; light grey is the curve after application of the outlier identification procedure described in section 4.3.2; and the dark grey curve is the Bayesian posterior probability distribution. Open data point symbols in panels 1–3 represented omitted data. Older detrital analyses beyond the scale of the age axes are not shown; refer to Supplementary Information Table S1 for these results.

4.4 **Tephrochronology: correlation to known-age tephra**

In addition to direct dating of feldspars recovered from tuffaceous zones within the Chew Bahir core (described in section 4.3, tephrochronometry), there is also the possibility of using tephrochronology to establish age-equivalence. In this approach, primary tephra (including cryptotephra) deposits found within the core are linked on the basis of their major and minor element geochemistry to known and directly-dated tephra found elsewhere, such as in sediment outcrops. Only one visible tephra unit was identified within the Chew Bahir cores. This and other potential (crypto)tephra-bearing zones were explored as described below.

4.4.1 *Tephrochronology Methods*

During the initial core description at LacCore, tuffaceous zones within core sections were noted and sedimentary features described. Smear slides were made to explore the depth range within which high concentrations of volcanic glass shards were present. Continuous and contiguous 10 cm samples were taken along the same interval to quantify and verify the distribution of volcanic glass shards using standard cryptotephra methods (Blockley et al., 2005; see Supplementary Information section 2, *Tephrochronology*).

Samples containing tephra were washed through a sieve at 25 μm to remove fine material, then studied using high-powered polarising light microscopy to describe glass shard morphologies, before being mounted in epoxy resin on a microprobe sample stub in preparation for geochemical analysis. Epoxy stub mounts were ground by hand to reveal glass shards in horizontal cross section and then polished using diamond pastes down to a 0.25 μm grade.

Single glass-shard element oxide compositions were measured by wavelength dispersive electron microprobe analyses (WDS-EPMA), using either the JEOL-8600 microprobe in the Research Laboratory for Archaeology and the History of Art, University of Oxford, or the Cameca SX100 electron microprobe facility in the Department of Earth Sciences, University of Cambridge. Analysis was run on both instruments using a 15 kV accelerating voltage, a 10 μm diameter defocussed beam, and a beam current of 6 nA (Jeol-8600) or 10 nA (Cameca SX100). Count times for most elements were 30 s, but only 10 s for Na and 60 s for Cl and P. The microprobe was calibrated against a suite of mineral and oxide standards and analyses quantified using the PAP absorption correction method. Intermittent analyses of the MPI-DING standards ATHO-G and St-Hs6/80-G (Jochum et al., 2005; Jochum et al., 2006) were run to check instrument accuracy and indicate precision (Supplementary Information section 2, *Tephrochronology*).

A single visible tephra horizon noted at ~75 mcd (sampled as CHB_T74.755) was correlated to a previously dated tephra deposit esewhere. The Chew Bahir tephra major and minor element compositions of CHB_T74.755 were compared against the published glass shard compositions of tephra from tuffs dated within sequences in southern Ethiopia to between 200 - 100 ka BP (Fig. 5). This interval provides a generous window around an estimate of the tephra age based on the core stratigraphy. Outcrop samples are typically subject to pedogenesis or other forms of weathering, leading to reduced alkali (Na_2O and K_2O) contents. For this reason, un-normalised major and minor element compositions are compared using bi-plot comparisons. In order to verify the correlation to a tuff with limited published glass EPMA data and under different analytical operating conditions, a sample of the 155 ± 7 ka Silver Tuff (Clark et al., 2003, updated for new standard age and decay constants from the original published age of 154 ka, to be consistent with other $^{40}Ar/^{39}Ar$ ages in this study; here, sample ETH18-14F) was collected directly from the Konso site (Fig. 1) in November 2018 following Katoh et al. (1996), then prepared and analysed under the same operating conditions and alongside the same set of secondary standard glasses. Details of the field location and sampling are included in Supplementary Information Fig. S2.

4.4.2 *Tephrochronology Results*

One visible tephra horizon was recorded in the core at ~75 mcd.

CHB_T74.755

In core section CHB-2B-38E-3A three defined lenses of medium-coarse and fine ash span the section depth from 76.5 - 62.0 cm (Supplementary Information Fig. S1), which is equivalent to a basal composite core depth of 74.755 mcd for the first appearance of this pure airfall ash unit. Immediately above this is an ~8 cm thick weathered unit comprised of a mixture of ash and silt. Cryptotephra counts indicate that fine ash is present in high concentration within the overlying 1.60 m of sediment, reflecting a long duration of ash deposition, from both direct airfall and catchment inputs. Glass shards are transparent, with platy to curvilinear morphologies, with maximum longest axes lengths of ~300 µm (SI Fig. S1).

Glass shards all have pantelleritic peralkaline rhyolite compositions with (un-normalised) SiO_2 values ranging from 70.8 - 69.0 weight (wt) %, Al_2O_3 from 7.9 - 9.6 wt %, FeO from 4.2 - 6.2 wt %, Na_2O from 4.5 - 5.9 wt % and K_2O from 3.4 - 4.5 wt %. Analytical totals ranged from 92.5 to 95.2 wt %. No correlation is seen between Na_2O content and totals, indicating that low totals are related to secondary hydration, magmatic water and volatile content, rather than Na loss due to glass alteration or analytical methods.

Correlation to the Silver Tuff (Konso)

Figure 5A shows CHB_T74.755 plotted against published single-glass shard EPMA compositions for four Main Ethiopian Rift peralkaline tuffs described and dated to within a 200 - 100 ka target window. Analytical conditions between studies vary, as does the apparent degree of weathering of the analysed samples. However, taken as an initial comparison, the plot indicates a potential correlation between the visible CHB_T74.755 layer and the Silver Tuff from Konso, as both samples show similar values and trends in major element concentrations.

Figure 5B compares the composition of CHB_T74.755 against our new WDS-EPMA of glass shards from the Silver Tuff (sample ETH18-14F) from Konso, whilst average values for major and minor element oxide compositions are given in Table 6. ETH18-14F has a pantelleritic composition in-line with CH_T74.755. Un-normalised SiO_2 values range from 68.7 - 71.1 wt %, Al_2O_3 from 7.9 - 10.2 wt %, FeO from 4.2 - 6.1 wt %, Na_2O from 1.8 - 3.4 wt % and K_2O from 4.0 - 4.4 wt %. All element oxides concentrations show a good match between the two datasets, with the exception of Na_2O, which is on average ~2.5 wt% lower in ETH18-14F than in CHB_T74.755. The reduced Na_2O content is reflected in reduced analytical totals, which vary from 90.0 to 93.4 wt % in ETH18-14F. We interpret this difference as resulting from post-depositional alteration and consequent Na-loss from glass in the Silver Tuff deposit at Konso, which is consistent with the high level of pedogenesis observed in the outcrop (Supplementary Information Fig. S2).

On the basis of the convergence of sample compositions shown in Fig. 5, we correlate CHB_T74.755 to the Silver Tuff at Konso. The Silver Tuff found at Konso has been $^{40}Ar/^{39}Ar$ dated to 155 ± 7 ka by Clark et al. (2003; updated herein) providing a precise isochron age for the Chew Bahir sediment record at ~75 mcd. This age is consistent (within 1 σ uncertainties) with the $^{40}Ar/^{39}Ar$ age of 172 ± 12 ka at ~69 mcd.

Establishing a link between the tephra found in the Chew Bahir core and in sediment outcrops elsewhere is important. Not only does the identification of the CHB_T74.755 tephra give us an age to add to the age-depth model for Chew Bahir, but regardless of the precise age it also provides an opportunity to potentially make an isochronous link between the core and key neighbouring archaeological sites, allowing direct association of fossils and tools with the contemporary environmental and climatic context provided by the Chew Bahir core. Further analysis of other tuffaceous zones within the core is therefore ongoing.

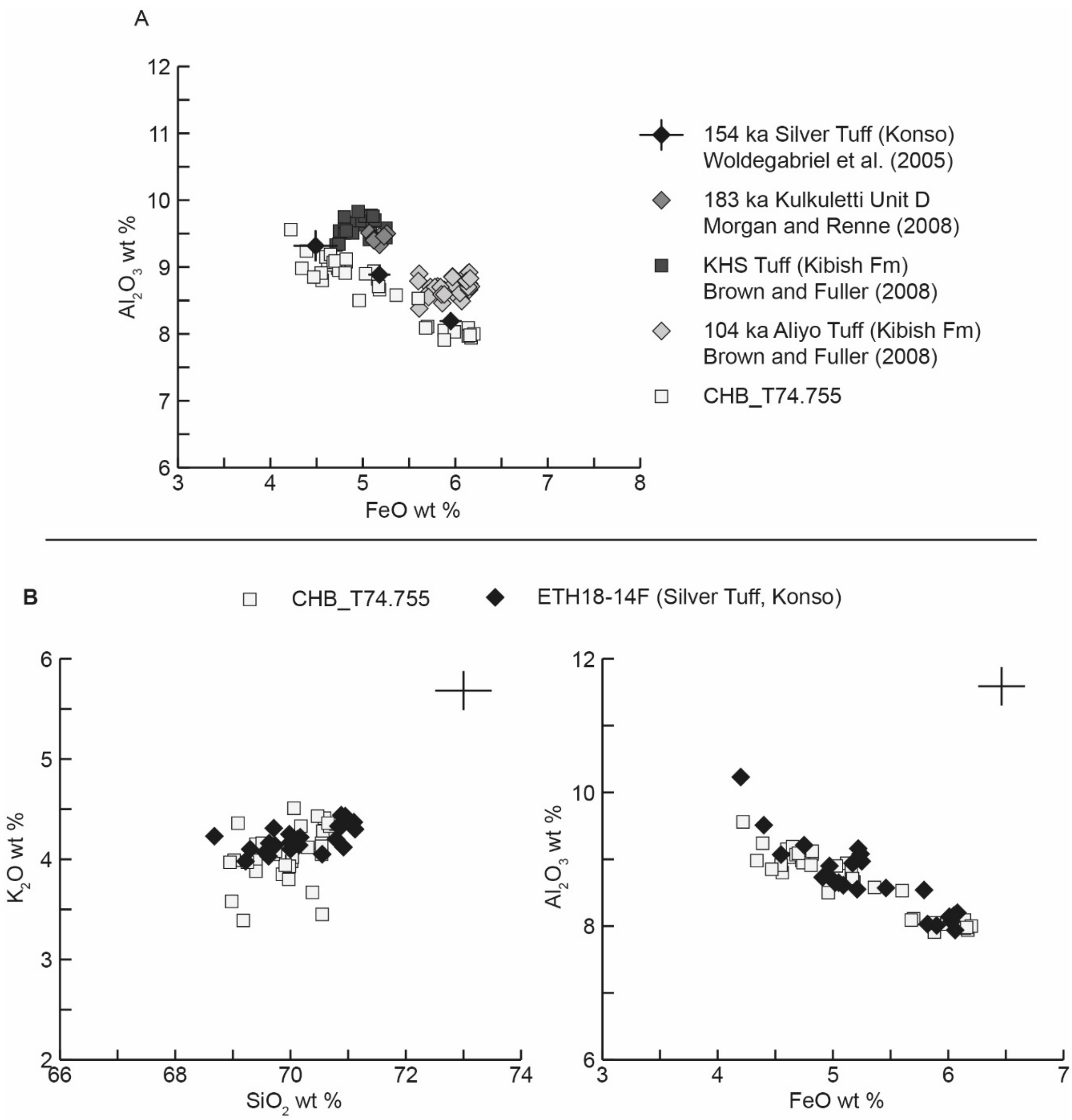

Figure 5: Selected bi-plots of tephra glass shard major element compositions illustrating the correlation of CHB_T74.755 to the Silver Tuff at Konso, reported by Clark et al. (2003; updated herin) as 155 ± 7 ka. Due to weathering and alkali-loss in exposed tuff units, data are plotted un-normalised, to avoid disproportionate inflation of element oxide concentrations. **A.** Comparison of CHB_T74.755 to published rhyolitic tuffs dated to 200 - 100 ka from

Roberts, H.M., Bronk Ramsey, C., Chapot, M.S., Deino, A.L., Lane, C.S., Vidal, C., Asrat, A., Cohen, A., Foerster, V., Lamb, H.F., Schäbitz, F., Trauth, M.H., Viehberg, F. (2021). Using multiple chronometers to establish a long, directy-dated lacustrine record: constraining >600,000 years of environmental change at Chew Bahir, Ethiopia. (Invited research article). Quaternary Science Reviews. DOI: 10.1016/j.quascirev.2021.107025

archaeological sites along the Main Ethiopian Rift. Single glass shard EPMA analyses are plotted for the 104 ± 7 ka Aliyo Tuff and KHS Tuff from the Kibish formation are from Brown and Fuller (2008); and for the 183 ± 10 ka Gademotta-Kulkuletti Unit D Tuff, from Morgan and Renne (2008). Silver Tuff data from WoldeGabriel et al. (2005) plotted as published mean and two sigma uncertainties for three EPMA datasets. **B.** Confirmation of the correlation of CHB_T74.755 to the Silver Tuff at Konso is demonstrated by comparison to single-grain tephra glass shard compositions of sample ETH18-14F, collected in this study, with samples analysed under the same instrumental operating conditions. Crosses indicate approximate two sigma analytical uncertainties, based on repeat analyses of homogenised volcanic glass standards (see also Supplementary Information Table S2).

5. Age-depth model using directly-dated samples

Section 4 discussed the ages generated for the Chew Bahir composite core using four independent chronologic techniques, namely radiocarbon, quartz OSL, ^{40}Ar/^{39}Ar dating, and tephrochronology. The radiocarbon, OSL, and ^{40}Ar/^{39}Ar chronometers were internally consistent, producing ages in chronostratigraphic order. The 30 ages can be combined in an age-depth model that takes into account the stratigraphic information for the direct dating samples and the core, and incorporates the different relative uncertainties associated with the ages generated, to provide an assessment of modelled age throughout the entire composite core. To that end, a Bayesian age-depth model (see Supplementary Information section 3) was created using OxCal v4.4.3 (Bronk Ramsey, 2009; 2017) using the Poisson *P_Sequence* model (Bronk Ramsey, 2008) which assumes an underlying random process of deposition which is uniform over long timescales. The age of the top of the sequence was fixed to 2014 CE, the year of coring. Radiocarbon dates were calibrated within OxCal using the IntCal20 calibration curve (Reimer et al., 2020); prior to this, allowance was made within the model for an unknown reservoir effect of between 0 and 3,000 years, giving a single reservoir offset value determined from the examination of multiple age determinations through the modelling process (Figure S3), applied to the radiocarbon ages prior to calibration.

The age-depth model based on direct dating gave an age of ~620 ka at the base of the core at ~293 mcd (Figure 6a). This gave an average sediment accumulation rate across the entire composite core of 0.47 mm/a, which lies between the values for average sediment accumulation rates at Lake Bosumtwi (western Africa) and Lake Malawi (southeastern Africa) (~0.4 - 0.5 mm/a, calculated using the data of Scholz et al., 2007 and Shanahan et al., 2013), and falling within the range of values observed at Lake Tana, Ethiopia (ranging from 0.37, 0.76 and 0.25 mm/a for the three seismic facies units identified at Lake Tana, and an overall average value of 0.35 mm/a across the 92 m Tana core as a whole; Roberts et al., 2018).

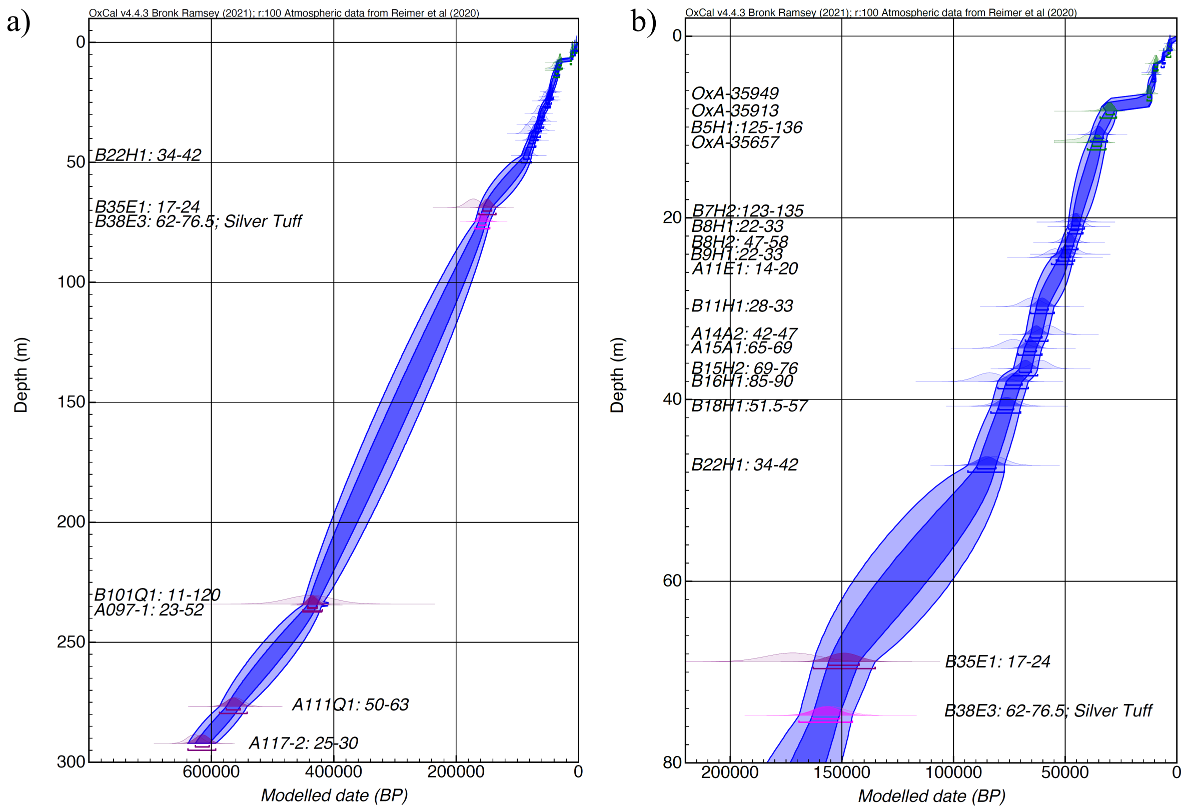

Figure 6: Bayesian age-depth model output for a) the full 293 m composite core from Chew Bahir, and b) the upper 80 m only. Individual ages used as model input are shown, with different colours used for ages generated by different techniques: radiocarbon (n=6) is shown in green, quartz OSL (n=18) in blue, $^{40}Ar/^{39}Ar$ (n=5) in purple, and the correlative tephra (n=1) is shown in magenta. The modelled ages are indicated by the continuous blue-shaded bands at 95% probability (light blue), and 68% probability (dark blue).

The information derived from direct dating of the core suggest that the composite core from Chew Bahir has both the duration (> 600 ka) and also the resolution (~10 years per 0.5 cm depth on average) to allow examination of some of the key questions related to past climate and environmental change and potential links to human evolution and migration. On closer examination (Fig. 6b), the ages derived from direct dating suggest that the accumulation rate and hence also the resolution of the record has varied over time, as might reasonably be expected over a timescale of more than 600 ka, and given the changes in stratigraphy outlined in Fig. 2. The Bayesian model output gives accumulation rates ranging from maxima of ~1.8 mm/a in parts of the upper few m of the core (notably at ~4m depth) to as low as ~0.1 mm/a elsewhere. These changes do not relate clearly to any notable changes in stratigraphy, and are only revealed by direct-dating of the sediments.

Perhaps the most notable change in accumulation rate is seen between ~8.5 to 6.5 mcd, where there is a dramatic reduction in sediment accumulation rate, or potentially a hiatus or an erosion event, occurring between ~30 to 12 ka (Fig. 6b). This time period includes the Last Glacial Maximum, and describes the entirety of marine isotope stage (MIS) 2. Quartz could not be recovered within this zone of the Chew Bahir sediment cores, but luminescence data from feldspars using a post-IR_{50} $IRSL_{225}$ signal which shows a progression in relative D_e values, L_n/T_n*T_D values and an increase in the ages of samples with increased depth through this relatively modest 2m of core sediments (data not shown), suggests that this is a time of dramatically reduced sediment accumulation rate (~0.1 mm/a) rather than a cessation of deposition or a loss of sediment via an erosive event. This, in turn, suggests a reduction of precipitation in this region during MIS 2, causing a reduction in runoff and sediment input to the lake basin. This observation is consistent with the marked decrease in precipitation or precipitation-minus-evaporation noted for much of the African continent during the Last Glacial Maximum (Gasse, 2000).

Viehberg et al. (2018) also found evidence for desiccation during the Last Glacial Maximum in their study of much shorter sediment cores taken from the central part of the Chew Bahir lake basin, based on sediment composition and lack of ostracod valves. Whilst further studies on short cores from sites within the lake basin (e.g. Foerster et al, 2012 and Trauth et al., 2015) report some calibrated radiocarbon dates consistent with MIS 2 and calculate sediment accumulation rates of ~0.1 mm/a between ~35 and ~15 ka, bracketed by sediments with higher accumulation rates of ~0.5 – 0.6 mm/a, which are consistent with the rates determined in the present paper for the composite core CHB14. Interestingly, the directly-dated 92 m sediment record of Lamb et al. (2018, their Fig. 3 and their SI Fig. 4) at Lake Tana, Ethiopia, suggests that either MIS 2 is entirely missing from the sedimentary record, or that the accumulation rate is extremely low leading to a highly compressed sequence during this time period and again inferring drier conditions during MIS 2. Several other independent sites in Ethiopia also demonstrate significant gaps in the sedimentological or archaeological record at this time, such as the caves of Goda Buticha in eastern Ethiopia (Tribolo et al., 2017; Pleurdeau et al., 2014), Porc-Epic (Leplongeon, 2014), and Ziway-Shala (Menard et al., 2014).

There may be other similar events that have impacted the accumulation of sediment in the Chew Bahir basin in a similar way to those noted for MIS 2. For example, a further period of slow sediment accumulation is noted in the Chew Bahir composite core between ~9.3 to 6.3 ka (Fig 6b), which may also imply dominantly dry conditions, and potentially corresponds to brief drier intervals identified by Foerster et al. (2012; 2015) and Fischer et al. (2020) within the otherwise prevailing humid conditions of the time. But as dense as the current direct dating record is for the Chew Bahir composite core, the dating resolution is still too low to be able to explore the presence of such events further using the current age-depth model, particularly with increasing depth as the dating resolution and the absolute precision in age decreases down core.

6. Summary and conclusions

The ~293 m composite sediment core from Chew Bahir was dated directly using multiple radiometric chronometers (radiocarbon, quartz OSL, and $^{40}Ar/^{39}Ar$ techniques) plus correlation on the basis of geochemistry of one tephra unit within the core to a dated tephra ('Silver Tuff') found in an archaeologically significant outcrop at Konso, about 80 km NE of the Chew Bahir core site. These four dating techniques are all independent, are applied to different materials associated with different chronologic events, and have diverse strengths and weaknesses within a lacustrine setting. The suite of 30 ages generated for the Chew Bahir core materials were chronostratigraphically consistent, giving additional confidence in the ages generated. The use of multiple independent chronometers with different age ranges permits coverage of the entire core. Bayesian modelling produced a coherent, internally-consistent age-depth model, and suggested that the composite core record spans ~620 ka of accumulation at the Chew Bahir site.

The mean accumulation rate across the ~293 m Chew Bahir core of 0.47 mm/a (based on the basal date) is consistent with other long lake records from Africa calculated in the same fashion (e.g. Lake Bosumtwi, Lake Malawi, and Lake Tana which have average accumulation rates of ~0.4 to ~0.5 mm/a). In practical terms, this means that large detailed datasets containing proxies for climate and environmental change, such as scanning micro-XRF or magnetic susceptibility data collected every 0.5 cm, correspond to a relatively high average resolution of ~10 years between datapoints over the last ~620 ka. However, direct dating of the core sediments reveals that the accumulation rate is not constant over time, and hence the resolution of the record varies accordingly. One of the most dramatic changes in accumulation rate is observed during MIS 2 when the calculated accumulation rate drops to 0.1 mm/a; luminescence data from feldspars suggests that this is due to a reduction in sediment supply rather than due to a hiatus in deposition or loss of material by significantly increased erosion. This observation is consistent with evidence from many locations elsewhere in eastern Africa, suggesting that the Last Glacial Maximum was a relatively dry period.

The ~293 m sediment sequence at Chew Bahir is one of the longest directly-dated records in eastern Africa, and the high resolution of the sedimentary record itself means that other large changes in accumulation rate may also have been recorded during the ~620 ka period of deposition. However, in spite of the relatively large number of ages generated, the resolution of the current Chew Bahir age-depth model applied to the sediments is not sufficient to allow such potential changes to be clearly identified, although there are suggestions of such fluctuations in the upper portions of the core where the density of ages increases. Further dating work will doubtless reveal yet more detail and allow the age-depth models to be refined further. Nevertheless, the rapid and dramatic changes in accumulation rate that have already been identified at Chew Bahir using the current age-depth model illustrate the benefits of direct dating over linear extrapolation or interpolation, with the inherent simplistic assumptions of constant accumulation rate that are necessitated by those approaches. Direct dating also allows the identification of events in the proxy record potentially related to climate and environmental drivers but without concerns regarding circularity of reasoning that can be associated with orbital tuning of stratigraphic records.

The use of multiple independent chronometric techniques adds confidence to the ages generated in any dating study (e.g. Shanahan et al., 2013), but this approach is particularly beneficial in lacustrine settings where no single dating technique is without complications. Using a Bayesian approach, knowledge of the stratigraphic relationships between a series of directly-dated samples can then be used to create modelled ages throughout the sedimentary sequence, and potentially refine the precision of the modelled ages compared to that of individual ages. Taking this approach at Chew Bahir using four independent chronometers is highly robust, and revealed the ~293 m CHB-14 composite core to be a high resolution directly-dated record spanning ~620 ka duration. Not only do the chronologic investigations presented in this study demonstrate for the first time that this composite core spans a critical time range of interest for studies of hominin evolution, adaptation and dispersal, but the chronology also reveals that the core is of sufficiently high resolution to allow further work on climate and environmental change at this climatically-sensitive location close to key fossil hominin sites.

Acknowledgements

We thank staff at the Oxford Radiocarbon Accelerator Unit, in particular Richard Staff, David Chivall and Victoria Cullen, as well as Patrick Robson for pollen and charcoal separation. Annett Junginger performed the fish bone collection during the "sampling party" at LacCore, Minneapolis, in spring 2015. We thank Anders Noren, Kristina Brady, Mark Shapley, and Brian Grivna, of LacCore for their support throughout the project. Victoria Cullen and Alma Piermattei provided technical assistance with tephra analyses; Victoria Smith and Iris Buisman gave support with EPMA. Hollie Wynne provided vital technical assistance in the Aberystwyth Luminescence Research Laboratory. We are grateful to Yonas Beyene who allowed us access to the Konso tephra localities. We acknowledge many local, regional and Federal authorities in Ethiopia for providing permits for scientific drilling in the Chew Bahir Basin, and for facilitating actual drilling operations as well as sample export. Céline Vidal was supported by a Leverhulme Trust grant (Nature and impacts of Middle Pleistocene volcanism in the Ethiopian Rift; 2016-20). The work described here is part of the Hominin Sites and Paleolakes Drilling Project (HSPDP) funded by grants from ICDP, NSF (EAR1338553; BCS-1322017; EAR-2020044), NERC (NE/K014560/1) and DFG (Priority Program SPP 1006; SCHA 472/13 and /18; TR 419/8, /10 and /16) and the CRC 806 Research Project number 57444011 "Our Way to Europe". This is publication #38 of the Hominin Sites and Paleolakes Drilling Project.

References

Aitken, M.J., 1985. Thermoluminescence Dating. Academic Press, London.

Banerjee, D., Murray, A. S., Bøtter-Jensen, L., Lang, A., 2001. Equivalent dose estimation using a single aliquot of polymineral fine grains. Radiation Measurements 33, 73-94.

Blockley, S.P.E., Pyne-O'Donnell, S.D.F., Lowe, J.J., Matthews, I.P., Stone, A., Pollard, A.M., Turney, C.S.M., Molyneux, E.G., 2005. A new and less destructive laboratory procedure for the physical separation of distal glass tephra shards from sediments. Quat. Sci. Rev. 24, 1952–1960.

Brock, F., Higham, T., Ditchfield, P. and Bronk Ramsey, C., 2010. Current pretreatment methods for AMS radiocarbon dating at the Oxford Radiocarbon Accelerator Unit (ORAU). Radiocarbon, 52(1), pp.103-112.

Bronk Ramsey, C., 2008. Deposition models for chronological records. Quaternary Science Reviews, 27(1-2), 42-60.

Bronk Ramsey, C., 2009. Bayesian analysis of radiocarbon dates. Radiocarbon, 51(1), 337-360.

Bronk Ramsey, C., 2017. Methods for Summarizing Radiocarbon Datasets. Radiocarbon, 59(2), 1809-1833.

Bronk Ramsey, C., Higham, T.F.G. and Leach, P., 2004. Towards High-Precision AMS: Progress and Limitations. Radiocarbon, 46(01), pp.17-24.

Brooks, A.S., Yellen, J.E., Potts, R., Behrensmeyer, A.K., Deino, A.L., Leslie, D.E., Ambrose, S.H., Ferguson, J.R., d'Errico, F., Zipkin, A.M., Whittaker, S., Post, J., Veatch, E.G., Foecke, K., Clark, J.B., 2018. Long-distance stone transport and pigment use in the earliest Middle Stone Age. Science 360 (6384), 90-94.

Brown, F.H., Fuller, C.R., 2008. Stratigraphy and tephra of the Kibish Formation, southwestern Ethiopia. J. Hum. Evol. 55, 366–403.

Brown, F. H., McDougall, I. & Fleagle, J. G., 2012. Correlation of the KHS Tuff of the Kibish Formation to volcanic ash layers at other sites, and the age of early Homo sapiens (Omo I and Omo II). Journal of Human Evolution 63, 577–585.

Burnett, A.P., Soreghan, M.J., Scholz, C.A., Brown, E.T., 2011. Tropical East African climate change and its relation to global climate: a record from Lake Tanganyika, Tropical East Africa, over the past 90þ kyr. Palaeogeography, Palaeoclimatology, Palaeoecology 303, 155-167.

Buylaert, J.P., Jain, M., Murray, A.S., Thomsen, K.J., Thiel, C., Sohbati, R., 2012. A robust feldspar luminescence dating method for Middle and Late Pleistocene sediments. Boreas 41, 435-451.

Campisano, C.J., Cohen, A.S., Arrowsmith, J.R., Asrat, A., Behrensmeyer, A.K., Brown, E.T., Deino, A.L., Deocampo, D.M., Feibel, C.S., Kingston, J.D., Lamb, H.F., Lowenstein, T.K., Noren, A., Olago, D.O., Owen, R.B., Pelletier, J.D., Potts, R., Reed, K.E., Renaut, R.W., Russell, J.M., Russell, J.L., Schäbitz, F., Stone, J.R., Trauth, M.H., Wynn, J.G., 2017. The Hominin Sites and Paleolakes Drilling Project: high-resolution paleoclimate records from the East African Rift System and their implications for understanding the environmental context of hominin evolution. PaleoAnthropology 2017, 1-43.

Clark, J.D., Beyene, Y., WoldeGabriel, G., Hart, W.K., Renne, P.R., Gilbert, H., Defleur, A., Suwa, G., Katoh, S., Ludwig, K.R., Boisserie, J.-R., Asfaw, B., White, T.D., 2003. Stratigraphic, chronological and behavioural contexts of Pleistocene Homo sapiens from

Middle Awash, Ethiopia. Nature 423, 747–752.

Chapot, M.S., Roberts, H.M., Duller, G.A.T., Lai, Z.P., 2012. A comparison of natural- and laboratory-generated dose response curves for quartz optically stimulated luminescence signals from Chinese Loess. Radiation Measurements 47, 1045-1052.

Cohen, A., Campisano, C., Arrowsmith, R., Asrat, A., Behrensmeyer, A.K., Deino, A., Feibel, C., Hill, A., Johnson, R., Kingson, J., Lamb, H., Lowenstein, T., Noren, A., Olago, D., Owen, R.B., Potts, R., Reed, K., Renaut, R., Schäbitz, F., Tiercelin, J.J., Trauth, M.H., Wynn, J., Ivory, S., Brady, K., O'Grady, R., Rodysill, J., Githiri, J., Russell, J., Foerster, V., Dommain, R., Rucina, S., Deocampo, D., Russell, J., Billingsley, A., Beck, C., Dorenbeck, G., Dullo, L., Feary, D., Garello, D., Gromig, R., Johnson, T., Junginger, A., Karanja, M., Kimburi, E., Mbuthia, A., McCartney, T., McNulty, E., Muiruri, V., Nambiro, E., Negash, E.W., Njagi, D., Wilson, J.N., Rabideaux, N., Raub, T., Sier, M.J., Smith, P., Urban, J., Warren, M., Yadeta, M., Yost, C., Zinaye, B., 2016. The Hominin Sites and Paleolakes Drilling Project: Inferring the Environmental Context of Human Evolution from Eastern African Rift Lake Deposits. Scientific Drilling 21, 1-16.

Dee, M. and Bronk Ramsey, C., 2000. Refinement of graphite target production at ORAU. Nuclear Instruments and Methods in Physics Research, B172(1–4), pp.449-453.

Deino, A.L., Behrensmeyer, A.K., Brooks, A.S., Yellen, J.E., Sharp, W.D., Potts, R., 2018. Chronology of the Acheulean to Middle Stone Age transition in eastern Africa. Science 360 (6384), 95-98.

Deino, A.L., Sier, M.J., Garello, D., Keller, B., Kingston, J., Scott, J., Dupont-Nivet, G., Cohen, A., 2019. Chronostratigraphy of the Baringo-Tugen-Barsemoi (HSPDP-BTB13-1A) Core – 40Ar/39Ar dating, magnetostratigraphy, tephrostratigraphy, sequence stratigraphy and Bayesian age modeling. Palaeogeography, Palaeoclimatology, Palaeoecology 532: A high resolution, multi-proxy record of Pliocene hominin environments in the Kenya Rift Valley: Analysis of the Baringo-Tugen-Barsemoi (BTB) Core, 109519.

Duesing, W., Berner, N., Deino, A.L., Foerster, V., Kraemer, H., Marwan, N., Trauth, M.H. (2021) Multiband wavelet age modeling (MUBAWA) for a ~293 m (~600 kyr) sediment core from Chew Bahir basin, southern Ethiopian Rift. Frontiers in Earth Science. doi: 10.3389/feart.2021.594047

Duller, G.A.T., 2003. Distinguishing quartz and feldspar in single grain luminescence measurements. Radiation Measurements 37, 161-165.

Fischer, M.L., Markowska, M., Bachofer, F., Foerster, V., Asrat, A., Zielhofer, C. Trauth, M.H., and Junginger, A., 2020. Determining the pace and magnitude of lake level changes in southern Ethiopia over the last 20,000 years using Lake Balance Modelling and SEBAL. Frontiers in Earth Science 8, 197. doi: 10.3389/feart.2020.00197.

Foerster, V., Junginger, A., Langkam, O., Gebru, T., Asrat, A., Umer, M., Lamb, H.F., Wennrich, V., Rethemeyer, J., Nowaczyk, N., Trauth, M.H., Schaebitz, F., 2012. Climatic change recorded in the sediments of the Chew Bahir basin, southern Ethiopia, during the last 45,000 years. Quaternary International 274, 25–37.

Foerster, V., Vogelsang, R., Junginger, A., Asrat, A., Lamb, H.F., Schaebitz, F., Trauth, M.H. (2015). Environmental change and human occupation of southern Ethiopia and northern Kenya during the last 20,000 years. Quaternary Science Reviews, 129, 333-340.

Foerster, V., Deocampo, D.M., Asrat, A., Günter, C., Junginger, A., Krämer, K.H., Stroncik, N.A., Trauth, M.H., (2018). Towards an understanding of climate proxy formation in the Chew Bahir basin, southern Ethiopian Rift. Palaeogeography, Palaeoclimatology, Palaeoecology, 501, 111-123.

Foerster, V. Asrat, A., Bronk Ramsey, C., Brown, E.T., Chapot, M.S., Deino, A., Deocampo, D.M., Düsing, W., Hahn, A., Junginger, A., Kaboth-Bahr, S., Lane, C.S., Noren, A., Roberts, H.M., Tiedemann, R., Vidal, C., Vogelsang, R., Cohen, A.S., Lamb, H.F., Schaebitz, F., Trauth, M.H. (submitted) ~620 kyrs of climate variability in eastern Africa has driven hominin evolution, innovation and dispersal. Nature.

Gasse, F, 2000. Hydrological changes in the African tropics since the Last Glacial Maximum. Quaternary Science Reviews 19, 189–211.

Gliganic, L.A., Jacobs, Z., Roberts, R.G., Domínguez-Rodrigo, M., Mabulla, A.Z.P., 2012. New ages for Middle and Later Stone Age deposits at Mumba rockshelter, Tanzania: optically stimulated luminescence dating of quartz and feldspar grains. Journal of Human Evolut 62, 533e547.

Groucutt, H.S., Petraglia, M.D., Bailey, G., Scerri, E.M.L., Parton, A., Clark-Balzan, L., Jennings, R.P., Lewis, L., Blinkhorn, J., Drake, N.A., Breeze, P.S., Inglis, R.H., Deves, M.H., Meredith-Williams, M., Boivin, N., Thomas, M.G., Scally, A., 2015. Rethinking the Dispersal of *Homo sapiens* out of Africa. Evolutionary Anthrolopology 24, 149-164.

Guérin, G., Mercier, N., Adamiec, G., 2011. Dose-rate conversion factors: update. Ancient TL 29, 5-8.

Hublin, J-J., Ben-Ncer, A., Bailey, S.E., Freidline, S.E., Neubauer, S., Skinner, M.M., Bergmann, I., Le Cabec, A., Benazzi, S., Harvati, K., Gunz, P., 2017. New fossils from Jebel Irhoud, Morocco and the pan-African origin of *Homo sapiens*. Nature 546, 289–292.

Jochum, K.P., Nohl, U., Herwig, K., Lammel, E., Stoll, B., Hofmann, A.W., 2005. GeoReM: a new geochemical database for reference materials and isotopic standards. Geostand. Geoanalytical Res. 29, 333–338.

Jochum, K.P., Stoll, B., Herwig, K., Willbold, M., Hofmann, A.W., Amini, M., Aarburg, S., Abouchami, W., Hellebrand, E., Mocek, B., 2006. MPI-DING reference glasses for in situ microanalysis: New reference values for element concentrations and isotope ratios. Geochemistry, Geophys. Geosystems 7.

Junginger, A., Trauth, M.H., 2013. Hydrological constraints of paleo-Lake Suguta in the Northern Kenya Rift during the African Humid Period (15e5 ka). Global and Planetary Change 111, 174-188.

Junginger, A., Roller, S., Trauth, M.H., 2014. The effect of solar irradiation changes on water levels in the paleo-Lake Suguta, Northern Kenya Rift, during the late Pleistocene African Humid Period (15 - 5 ka BP). Palaeogeography, Palaeoclimatology, Palaeoecology, 396, 1-16.

Katoh, S., Nagaoka, S., WoldeGabriel, G., Beyene, Y., Suwa, G., 1996. Preliminary study on geomorphological development since the early Pleistocene in Konso-Gardula area (KGA), southern Ethiopia. Proc. Gen. Meet. Assoc. Jpn. Geogr. 49, 208–209.

Keller, C.B., Schoen, B., Samperton, K.M., 2018. A stochastic sampling approach to zircon eruption age interpretation. Geochemical Perspectives Letters 8, 31-35.

Lamb, H.F., Bates, C. R., Bryant, C. L., Davies, S., Huws, D. G., Marshall, M. H., Roberts, H. M. and Toland, H., 2018. 150,000-year palaeoclimate record from northern Ethiopia supports early, multiple dispersals of modern humans from Africa. Scientific Reports 8, 1077.

Lane, C.S., Chorn, B.T., Johnson, T.C., 2013. Ash from the Toba supereruption in Lake Malawi shows no volcanic winter in East Africa at 75 ka. Proceedings of the National Academy of Sciences, 110 (20), 8025-8029.

Lee, J.Y., Marti, K., Severinghaus, J.P., Kawamura, K., Yoo, H.S., Lee, J.B., Kim, J.S., 2006. A redetermination of the isotopic abundances of atmospheric Ar. Geochim. Cosmochim. Acta 70, 4507-4512.

Leplongeon, A., 2014. Microliths in the Middle and Later Stone Age of eastern Africa: New data from Porc-Epic and Goda Buticha cave sites, Ethiopia. Quaternary International 343, 100-116.

Li, B., Jacobs, Z., Li, S-H, Roberts, R.G., 2014. Review and assessment of the potential of post-IR IRSL dating methods to circumvent the problems of anomalous fading in feldspar luminescence. Geochronometria 41, 178-201.

Mauz, B., Packman, S., Lang, A., 2006. The alpha effectiveness in silt-sized quartz: New data obtained by single and multiple aliquot protocols. Ancient TL 24, 47-52.

McDougall, I., Brown, F.H., Fleagle, J.G., 2005. Stratigraphic placement and age of modern humans from Kibish, Ethiopia. Nature 433, 733 - 736.

McDougall, I., Brown, F. H., Fleagle, J. G., 2008. Sapropels and the age of hominins Omo I and II, Kibish, Ethiopia. Journal of Human Evolution 55, 409–420.

Min K., Mundil R., Renne P. R., Ludwig K. R., 2000. A test for systematic errors in ^{40}Ar/^{39}Ar geochronology through comparison with U–Pb analysis of a 1.1 Ga rhyolite. Geochim.Cosmochim. Acta 64, 73–98.

Ménard, C., Bon, F., Dessie, A., Bruxelles, L., Douze, K., Fauvelle, F.-X., Khalidi, L., Lesur, J., Mensan, R., 2014. Late Stone Age variability in the Main Ethiopian Rift: New data from the Bulbula River, Ziway-Shala basin. Quaternary International 343, 53-68.

Morgan, L.E., Renne, P.R., 2008. Diachronous dawn of Africa's Middle Stone Age: new ^{40}Ar/^{39}Ar ages from the Ethiopian Rift. Geology 36, 967–970.

Nicholson, S.E., 2017. Climate and climatic variability of rainfall over eastern Africa. Reviews of Geophysics, 55, 590-635.

Niespolo, E.M., Rutte, D., Deino, A.L., Renne, P.R., 2017. Intercalibration and age of the Alder Creek sanidine ^{40}Ar/^{39}Ar standard. Quaternary Geochronology 39, 205–213.

Owen, R.B., Muiruri, V.M., Lowenstein, T.K., Renaut, R.W., Rabideaux, N., Luo, S., Deino, A.L., Sier, M.J., Dupont-Nivet, G., McNulty, E.P., Leet, K., Cohen, A., Campisano, C., Deocampo, D., Shen, C.-C., Billingsley, A., Mbuthia, A., 2018. Progressive aridification in East Africa over the last half million years and implications for human evolution. Proceedings of the National Academy of Sciences 115, 11174-11179.

Pleurdeau, D., Hovers, E., Assefa, Z., Asrat, A., Pearson, O., Bahain, J-J, Lam, Y.M., 2014. Cultural change or continuity in the late MSA/Early LSA of southeastern Ethiopia? The site of Goda Buticha, Dire Dawa area. Quaternary International 343, 117–35.

Potts, R., Behrensmeyer, A.K., Faith, J.T., Tryon, C.A., Brooks, A.S., Yellen, J.E., Deino, A.L., Kinyanjui, R., Clark, J.B., Haradon, C.M., Levin, N.E., Meijer, H.J.M., Veatch, E.G., Owen, R.B., Renaut, R.W., 2018. Environmental dynamics during the onset of the Middle Stone Age in eastern Africa. Science 360 (6384), 86-90.

Prescott, J.R. and Hutton, J.T., 1988. Cosmic ray and gamma ray dosimetry for TL and ESR. Nuclear Tracks and Radiation Measurements 14, 223-227.

Prescott, J. R., Hutton, J. T., 1994. Cosmic ray contributions to dose rates for luminescence and ESR dating: large depths and long-term time variations. Radiation Measurements 23, 497-500.

Rees-Jones, J., 1995. Optical dating of young sediments using fine-grain quartz. Ancient TL 13, 9-14.

Reimer, P., Austin, W., Bard, E., Bayliss, A., Blackwell, P., Bronk Ramsey, C., Butzin, M., Cheng, H., Edwards, R., Friedrich, M., Grootes, P., Guilderson, T., Hajdas, I., Heaton, T., Hogg, A., Hughen, K., Kromer, B., Manning, S., Muscheler, R., Palmer, J., Pearson, C., van der Plicht, J., Reimer, R., Richards, D., Scott, E., Southon, J., Turney, C., Wacker, L., Adolphi, F., Büntgen, U., Capano, M., Fahrni, S., Fogtmann-Schulz, A., Friedrich, R., Köhler, P., Kudsk, S., Miyake, F., Olsen, J., Reinig, F., Sakamoto, M., Sookdeo, A., Talamo, S., 2020. The IntCal20 Northern Hemisphere radiocarbon age calibration curve (0–55 cal kBP). Radiocarbon, 62 (4), 725-757.Roberts, H.M., 2007. Assessing the effectiveness of the double-SAR protocol in isolating a luminescence signal dominated by quartz. Radiation Measurements, 42, 1627-1636.

Roberts, H.M., 2008. The development and application of luminescence dating to loess deposits: a perspective on the past, present, and future. Boreas 37, 483-507.

Roberts, H.M., Bryant, C.L., Huws, D.G., Lamb, H.F., 2018. Generating long chronologies for lacustrine sediments using luminescence dating: a 250,000 year record from Lake Tana, Ethiopia. Quaternary Science Reviews 202, 66-77.

Roberts, H.M., Duller, G.A.T., 2004. Standardised growth curves for optical dating of sediment using multiple-grain aliquots, Radiation Measurements 38, 241-252.

Schäbitz, F., Asrat, A., Lamb, H.F., Cohen, A., Foerster, V., Duesing, W., Kaboth-Bahr, S., Opitz, S., Viehberg, F., Vogelsang, R., Dean, J., Lang, M., Junginger, A., Bronk Ramsey, C., Chapot, M., Deino, A., Lane, C., Roberts, H.M., Vidal, C., Tiedemann, R., Trauth, M.H., (in review). Paleo-hydroclimate fluctuations in southern Ethiopia and possible implications for *Homo sapiens*. Nature Communications Earth & Environment.

Scholz, C.A., Johnson, T.C., Cohen, A.S., King, J.W., Peck, J.A., Overpeck, J.T., Talbot, M.R., Brown, E.T., Kalindekafe, L., Amoako, P.Y.O., Lyons, R.P., Shanahan, T.M., Castañeda, I.S., Heil, C.W., Forman, S.L., McHargue, L.R., Beuning, K.R., Gomez, J., Pierson, J., 2007. East African megadroughts between 135 and 75 thousand years ago and bearing on early-modern human origins. Proceedings of the National Academy of Sciences 104, 16416-16421.

Shanahan, T.M., Peck, J.A., McKay, N., Heil, C.W., King, J., Forman, S.L., Hoffmann, D.L., Richards, D.A., Overpeck, J.T., Scholz, C.A., 2013. Age models for long lacustrine sediment records using multiple dating approaches – an example from Lake Bosumtwi, Ghana. Quaternary Geochronology 15, 47-60.

Sier, M.J., Langereis, C.G., Dupont-Nivet, G., Feibel, C.S., Joordens, J.C., van der Lubbe, J.H., Beck, C.C., Olago, D., Cohen, A., 2017. The top of the Olduvai Subchron in a high-resolution magnetostratigraphy from the West Turkana core WTK13, hominin sites and Paleolakes Drilling Project (HSPDP). Quaternary Geochronology 42, 117-129.

Soares, P., Alshamali, F., Pereira, J.B., Fernandes, V., Silva, N.M., Alfonso, C., Costa, M.D., Musilova, E., Macaulay, V., Richards, M.B., Černý, V., Pereira, L., 2012. The expansion of mtDNA haplogroup L3 within and out of Africa. Molecular Biology and Evolution 29, 915-927.

Stringer, C., Galway-Witham, J., 2018. When did modern humans leave Africa? Science 359, 389-390.

Trauth, M.H., Bergner, A.G.N., Foerster, V., Junginger, A., Maslin, M.A., Schaebitz, F., 2015. Episodes of Environmental Stability and Instability in Late Cenozoic Lake Records of Eastern Africa. Journal of Human Evolution 87:21-31.

Trauth, M. H., Asrat, A., Cohen, A., Duesing, W., Foerster, V., Kaboth-Bahr, S., Kraemer, H., Lamb, H., Marwan, N., Maslin, M., Schaebitz, F., 2021. Recurring types of variability and transitions in the ~620 kyr record of climate change from the Chew Bahir basin, southern Ethiopia, Quaternary Science Reviews. doi: 10.1016/j.quascirev.2020.106777.

Tribolo, C., Asrat, A., Bahain, J-J., Chapon, C., Douville, E., Fragnol, C., Hernandez, M., Hovers, E., Leplongeon, A., Martin, L., Pleurdeau, D., Pearson, O., Puaud, S., Assefa, Z., 2017. Across the Gap: Geochronological and Sedimentological Analyses from the Late Pleistocene-Holocene Sequence of Goda Buticha, Southeastern Ethiopia. PLoS ONE 12(1): e0169418. doi:10.1371/journal.pone.0169418

Viehberg, F.A., Just, J., Dean, J.R., Wagner, B., Franze, S.O., Klasen, N., Kleinen, T., Ludwigh, P., Asrat, A., Lamb, H.F., Leng, M.J., Rethemeyer, J., Milodowski, A.E., Clausseng, M., Schäbitz, F., 2018. Environmental change during MIS4 and MIS 3 opened corridors in the Horn of Africa for Homo sapiens expansion. Quaternary Science Reviews 202, 139-153.

Wintle, A.G., Murray, A.S., 2006. A review of quartz optically stimulated luminescence characteristics and their relevance in single-aliquot regeneration dating protocols. Radiation Measurements 41, 369–391.

WoldeGabriel, G., Hart, W.K., Katoh, S., Beyene, Y., Suwa, G., 2005. Correlation of Plio–Pleistocene Tephra in Ethiopian and Kenyan rift basins: Temporal calibration of geological features and hominid fossil records. J. Volcanol. Geotherm. Res. 147, 81–108.

Labcode	Sample	^{14}C date (BP)	Error (1 σ)	δ^{13}C	Yield (mg)	Carbon (mgC)	Carbon (%)
OxA-X-2701-16	CHB14-2A-7E-2 (2-4 cm)	28600	750	-14.9	232.24	0.3772	3.3

Table 1: Radiocarbon date measured on pollen concentrate from the lake core. This was the only level where enough material was recovered to attempt this approach and, given the low carbon percentage this method was not pursued further.

Labcode	Sample	^{14}C date (BP)	Error (1 σ)	δ^{13}C	Yield (mg)	Carbon (mgC)	Carbon (%)
OxA-X-2705-25	CHB14-2A-11E-1 (74-76 cm)	26400	310	-17.2	5.31	0.7558	15.2

Table 2: Radiocarbon date measured on extracted charcoal from the core. This sample was taken from the level thought most likely to yield results by this method but the low carbon content and the mixed nature of the extract showed that this was not likely to be a reliable method to use here.

Labcode	Core Section (prefix CHB2014-)	Sample mid-point depth (cm)	Ostracod sample No.	Depth (mcd)	Measured date		Corrected date		δ^{13}C	Weight (mg)	Carbon (mg)
					^{14}C date (BP)	Error (1 σ)	^{14}C date (BP)	Error (1 σ)			
OxA-X-2731-50	2B-1-1	97	77	1.25	5390	120	5449	138	-4.9	2.4	0.049
OxA-35948*	2B-1-2	1	78	1.55	4830	55	4882	75	-0.6	21.9	0.153
OxA-35974*	2B-2-1	28	82	3.046	9779	37	9933	160	-3.1	35.0	0.981
OxA-35912*	2A-3-1	34	4	4.264	10511	38	10687	182	-2.7	59.5	2.182
OxA-35949*	2A-4-1	3	11	6.359	11900	75	12123	238	-0.3	3.7	0.190
OxA-35913*	2B-4-1	148	88	8.252	25800	100	27501	1897	3.7	55.7	2.359
OxA-35657*	2B-5-2	69	96	11.745	30640	150	34164	4427	1.6	36.9	1.395
OxA-X-2731-53	2B-9-1	52	118	24.233	29500	500	32466	3645	-2.2	3.3	0.065
OxA-35951	2B-38-3	37	182	74.435	38840	390			0.8	26.5	0.340

Roberts, H.M., Bronk Ramsey, C., Chapot, M.S., Deino, A.L., Lane, C.S., Vidal, C., Asrat, A., Cohen, A., Foerster, V., Lamb, H.F., Schäbitz, F., Trauth, M.H., Viehberg, F. (2021). Using multiple chronometers to establish a long, directy-dated lacustrine record: constraining >600,000 years of environmental change at Chew Bahir, Ethiopia. (Invited research article). Quaternary Science Reviews. DOI: 10.1016/j.quascirev.2021.107025

Table 3: Radiocarbon dates from ostracods recovered from the core. The table shows the core sections and the ostracod sample number. Depths shown here are expressed as metres composite depth (mcd). The corrections applied to the radiocarbon dates are explained in the text. The corrected dates for samples marked with an asterisk (*) were included in the direct dating age-depth model presented in this paper.

Table 4: Equivalent dose, dose rate, and optically stimulated luminescence ages for fine-grained quartz (4 - 11 µm diameter grains) prepared from Chew Bahir, Ethiopia.

ALRL Sample No. [a]	*Composite depth (m)*	*Equivalent Dose, D_e (Gy)*[b]	*No. aliquots used for D_e*	*Water content*[c]	*Alpha dose rate (Gy/ka)*[d]	*Beta dose rate (Gy/ka)*[d]	*Gamma dose rate (Gy/ka)*[d]	*Cosmic dose rate (Gy/ka)*[e]	*Total dose rate (Gy/ka)*[d]	*Quartz OSL Age (ka)*[f]
2B-1E-1: 45-62	0.815 ± 0.085	6.38 ± 0.91	18	23 ± 10	0.13 ± 0.02	1.23 ± 0.13	0.58 ± 0.06	0.093 ± 0.002	2.03 ± 0.14	3.15 ± 0.50
2B-1E-2: 69-79	2.280 ± 0.050	7.03 ± 0.08	6	74 ± 10	0.09 ± 0.01	0.66 ± 0.05	0.36 ± 0.03	0.082 ± 0.002	1.20 ± 0.06	5.87 ± 0.29
2A-2E-1: 36.5-54.5	2.683 ± 0.090	7.88 ± 0.09	18	76 ± 10	0.10 ± 0.02	0.66 ± 0.05	0.36 ± 0.03	0.077 ± 0.003	1.21± 0.06	6.53 ± 0.32
2B-2E-2: 15-30	3.996 ± 0.075	23.66 ± 0.60	8	45 ± 10	0.12 ± 0.02	1.24 ± 0.11	0.58 ± 0.05	0.069 ± 0.002	2.01 ± 0.12	11.76 ± 0.76
2A-3H-1: 28-40	4.251 ± 0.060	15.91 ± 0.22	12	52 ± 10	0.13 ± 0.02	0.94 ± 0.08	0.48 ± 0.04	0.063 ± 0.001	1.61 ± 0.09	9.88 ± 0.56
2B-5H-1: 125-136	10.860 ± 0.055	77.03 ± 0.90	12	24 ± 10	0.18 ± 0.03	1.37 ± 0.14	0.58 ± 0.03*	0.039 ± 0.001	2.16 ± 0.15	35.73 ± 2.44
2B-7H-2: 123-135	20.458 ± 0.060	94.00 ± 2.65	6	36 ± 10	0.14 ± 0.02	1.28 ± 0.12	0.63 ± 0.06	0.028 ± 0.001	2.08 ± 0.13	45.30 ± 3.19
2B-8H-1: 22-33	20.986 ± 0.055	83.95 ± 0.55	12	54 ± 10	0.12 ± 0.02	1.20 ± 0.10	0.57 ± 0.05	0.028 ± 0.000	1.91 ± 0.11	43.95 ± 2.55
2B-8H-2: 47-58	22.733 ± 0.055	76.83 ± 0.47	12	44 ± 10	0.13 ± 0.02	0.93 ± 0.08	0.50 ± 0.05	0.026 ± 0.000	1.59 ± 0.10	48.35 ± 2.91
2B-9H-1: 22-33	23.988 ± 0.055	87.39 ± 0.75	18	30 ± 10	0.13 ± 0.02	1.14 ± 0.11	0.53 ± 0.05	0.024 ± 0.000	1.83 ± 0.12	47.81 ± 3.27
2A-11E-1: 14-20	24.373 ± 0.030	117.84 ± 2.75	9	28 ± 10	0.19 ± 0.03	1.27 ± 0.13	0.68 ± 0.07	0.022 ± 0.001	2.16 ± 0.15	54.63 ± 3.89
2B-11H-1: 28-33	29.761 ± 0.025	113.01 ± 0.58	18	36 ± 10	0.12 ± 0.02	1.09 ± 0.10	0.51 ± 0.05	0.019 ± 0.000	1.74 ± 0.11	64.95 ± 4.23
2A-14A-2: 42-47	32.824 ± 0.025	107.62 ± 2.97	18	36 ± 10	0.13 ± 0.02	1.17 ± 0.11	0.56 ± 0.05	0.016 ± 0.000	1.87 ± 0.12	57.43 ± 4.06
2A-15A-1: 65-69	34.344 ± 0.020	148.77 ± 0.84	18	28 ± 10	0.14 ± 0.02	1.26 ± 0.12	0.61 ± 0.06	0.015 ± 0.000	2.03 ± 0.14	73.36 ± 5.08
2B-15H-2: 69-76	36.622 ± 0.035	114.88 ± 1.37	18	34 ± 10	0.16 ± 0.03	1.11 ± 0.10	0.60 ± 0.06	0.014 ± 0.000	1.88 ± 0.12	61.10 ± 4.06
2B-16H-1: 85-90	38.019 ± 0.025	154.74 ± 3.18	6	24 ± 10	0.21 ± 0.03	1.03 ± 0.11	0.59 ± 0.06	0.013 ± 0.000	1.84 ± 0.13	84.00 ± 6.00

2B-18H-1: 51.5-57	40.726 ± 0.027	152.69 ± 1.32	18	32 ± 10	0.19 ± 0.03	1.17 ± 0.11	0.64 ± 0.06	0.012 ± 0.000	2.00 ± 0.13	76.19 ± 4.95
2B-22H-1: 34-42	47.229 ± 0.040	129.77 ± 1.93	18	37 ± 10	0.17 ± 0.03	0.91 ± 0.08	0.51 ± 0.05	0.010 ± 0.000	1.59 ± 0.10	81.46 ± 5.26

[a] Aberystwyth Luminescence Research Laboratory (ALRL) sample prefix code: Aber-222/HSPDP-CHB14-

[b] The D_e is calculated using the weighted mean, and the error calculated is the standard error on the mean.

[c] Water content is expressed as the % of dry mass of sediment, and derived from the measured water content values.

[d] Alpha, beta, and gamma dose rate values (Gy/10^3yr) were determined from laboratory measurements using thick source alpha counting and beta counting, corrected for water content and grain size, and are shown to two decimal places. The conversion factors of Guerin et al. (2011) were used, and an a-value of 0.03 ± 0.003 was assumed (Rees-Jones, 1995; Mauz et al., 2006). For sample 2B-5H-1: 125-136, denoted *, the calculated gamma dose rate included a contribution from a stratigraphic unit ~ 5.5 cm from the unit the OSL dating sample was taken from, calculated using the approach outlined in Appendix H of Aitken (1985). All other samples in this table were taken ≥ 30 cm from any change of stratigraphic unit. Total dose rates are shown rounded to three decimal places, although the total dose rates and ages were calculated prior to rounding.

[e] The contribution from cosmic rays was calculated according to Prescott and Hutton (1994), using a water depth of 10 m overlying the sediment depth down-core, and assigned an uncertainty of 10%.

[f] Fine grain (4-11 µm) quartz OSL ages are calculated prior to rounding, expressed as thousands of years before 2015 AD, and shown to three significant figures.

Sample name (Prefix: CHB14-)	Tuff Unit name	Tuff Unit depth (mcd*)	^{40}Ar/^{39}Ar age (ka)
2B-035E-1 17-19 2B-035E-1 20-24	2B-035-1	68.855	172 ± 12
2B-101Q-1 11-35 2B-101Q-1 49-72 2B-101Q-1 72-94 2B-101Q-1 104-120	2B-101-1	234.067	438 ± 37
2A-097Q-1 23-34 2A-097Q-1 34-48 2A-097Q-1 48-52	2A-097-1	234.480	428.2 ± 7.7
2A-111Q-1 50-58 2A-111Q-1 61-63	2A-111-1	276.725	561 ± 14
2A-117Q-2 25-30	2A-117-2	292.118	628 ± 12

*mcd - metres composite depth

Table 5: ^{40}Ar/^{39}Ar ages of Chew Bahir (CHB14-) tuffaceous units. Note that the sample names shown indicate the depth intervals within each core run spanned by each sample e.g. for sample 2A-117Q-2 25-30, the sample was taken from 25-30 cm depth down that particular core section. The equivalent depth (mcd*) down the total composite core length is also shown for each sample listed.

		SiO2	TiO2	Al2O3	FeO	MnO	MgO	CaO	Na2O	K2O	P2O5	Cl	Total
						wt %						ppm	wt %
CHB_T74.755	**n=34**	**69.96**	**0.31**	**8.67**	**5.15**	**0.25**	**0.02**	**0.22**	**5.13**	**4.06**	**0.01**	**1365**	**93.94**
	2σ	*1.13*	*0.07*	*0.95*	*1.25*	*0.11*	*0.04*	*0.04*	*0.73*	*0.54*	*0.03*	*637*	*1.31*
ETH18-14F (Silver Tuff)	**n=25**	**70.14**	**0.32**	**8.67**	**5.32**	**0.29**	**0.01**	**0.23**	**2.66**	**4.20**	**0.01**	**1567**	**92.05**
	2σ	*1.33*	*0.06*	*1.09*	*1.11*	*0.09*	*0.01*	*0.04*	*0.89*	*0.24*	*0.02*	*647*	*1.91*

Table 6: Average of single-glass shard major and minor element oxide compositions for CHB_T74.755 and ETH18-14F measured by WDS-EPMA. Two sigma ranges indicate measured intra-population variation. Instrumental precision is indicated by replica secondary glass standard analyses, shown in Fig. 5B and SI Table S2.

Supplementary Information section S1: Tephrochronometry

Table S1: $^{40}Ar/^{39}Ar$ data (Excel file)

Supplementary information section S2: Tephrochronology

Methods of cryptotephra analyses

Prior to processing, samples for cryptotephra were dried at 105°C and weighed. Each sample weighed between 0.7 - 1.5 g. Dried samples were treated with 1 mol. HCl to remove any carbonates, then sieved through a 25 µm disposable nylon mesh to remove the finest particles. The > 25 µm fraction was further differentiated by density, using the heavy liquid sodium polytungstate (SPT) to first remove any organic material (< 1.95 g/cm^3) and then separating off any heavy-minerals below 2.55 g/cm^3. The resultant >25 µm and 1.95 - 2.55 g/cm^3 residue was mounted in Canada Balsam for inspection under high powered polarised light microscopy. Extracted residues containing > 95 % tephra glass shards are noted as having high ash content and for sample where the concentration of glass shards dropped below ~95 % of the mounted grains, shards were counted and quantified as shards per gram dry sediment (s/g) to provide an indication of the first and last appearance of ash in the core. Shard count distributions in core CHB-2B-38E support the position of the CHB_T74.755 isochron at the sharp base of the lowermost coarse airfall unit, equivalent to 74.755 mcd (Fig. S1).

Sample descriptions

Supplementary Information Figures S1 and S2 show the sedimentary contexts for tephra layers CHB_T74.755, within the Chew Bahir sediment core, and ETH18-14F, collected in the field from the Konso Formation in November 2018.

WDS-EPMA data

Complete and untransformed WDS-EPMA data from both tephra CHB_T74.755 from the Chew Bahir sequence and for the ETH18-14F sample of the Silver Tuff from Konso are shown in Table S2. The data are pre-filtered to remove accidental hits on non-tephra shard particles.

WDS-EPMA Secondary standard analyses

The homogenised volcanic glass secondary standards, Atho-G and StHs6/80-G, from the MPI-DING collection (Jochum et al., 2006) were analysed intermittently during both WDS-EPMA runs (on both the JEOL-8600 microprobe in the Research Laboratory for Archaeology and the History of Art, University of Oxford, and the Cameca SX100 electron microprobe facility in the Department of Earth Sciences, University of Cambridge). Secondary standard analyses are presented in SI Table S2 as mean and two standard deviation (2σ) values, alongside preferred compositional values from the GeoRem database (Jochum et al., 2005), indicating the accuracy of our analyses. The 2σ ranges on secondary standard glasses are used to calculate an indicative 2σ uncertainty for each element oxide composition plotted within bi-plots in Figure 5, panel B.

Fig S1: Core log and image showing the sedimentary context, structure and glass shard concentration of CHB_T74.755 within core CHB-2B-38E-3, along with photomicrograph of volcanic glass shards.

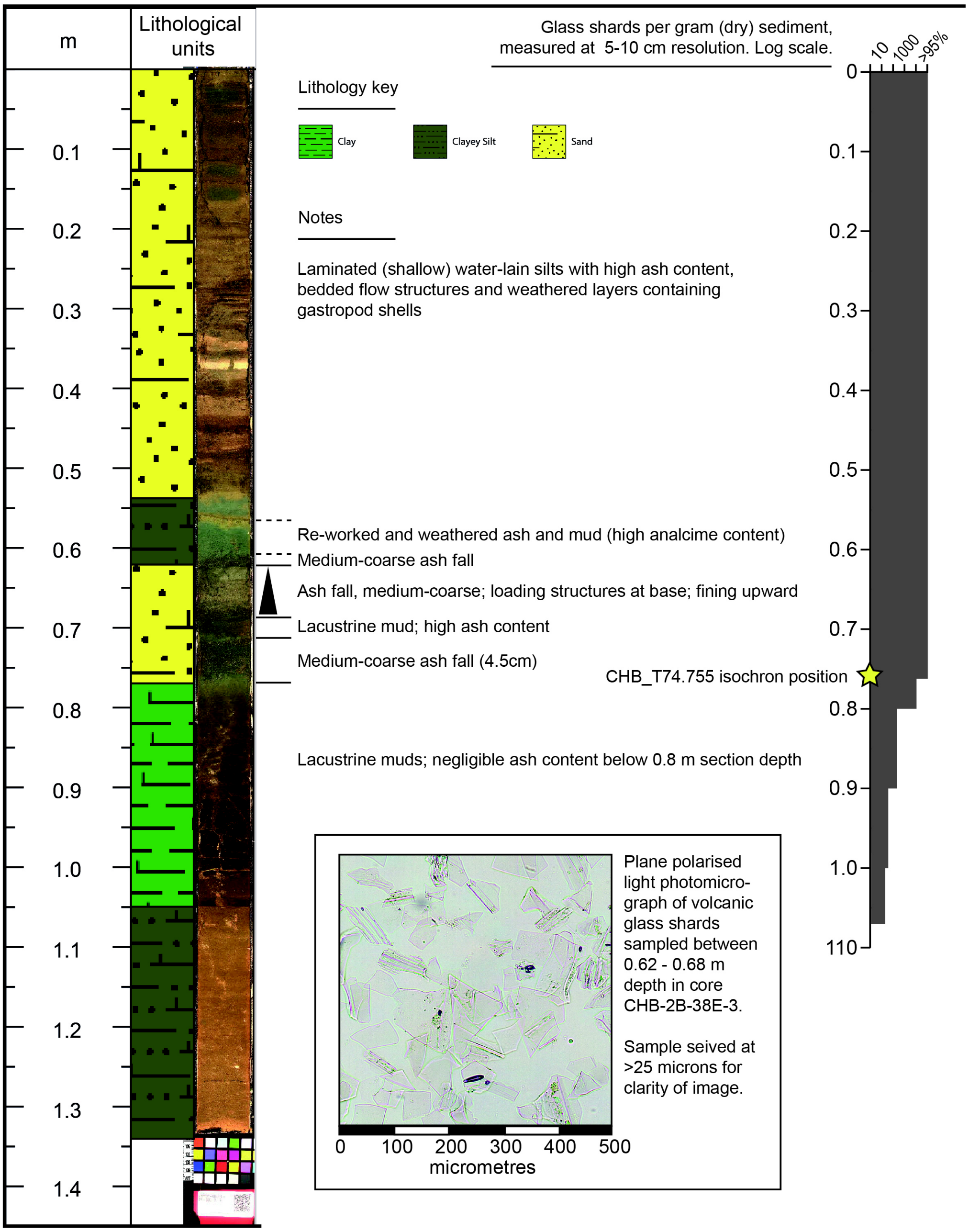

Roberts, H.M., Bronk Ramsey, C., Chapot, M.S., Deino, A.L., Lane, C.S., Vidal, C., Asrat, A., Cohen, A., Foerster, V., Lamb, H.F., Schäbitz, F., Trauth, M.H., Viehberg, F. (2021). Using multiple chronometers to establish a long, directy-dated lacustrine record: constraining >600,000 years of environmental change at Chew Bahir, Ethiopia. (Invited research article). Quaternary Science Reviews. DOI: 10.1016/j.quascirev.2021.107025

Fig S2: The Silver Tuff outcrop (TA-54 after Katoh et al. (1996), in the Upper Terrace of the Konso Formation (5.4162 N, 37.36219, 1428 m a.s.l.), sampled in November 2018 by Asfawossen Asrat, Christine Lane, Céline Vidal and Alan Deino.

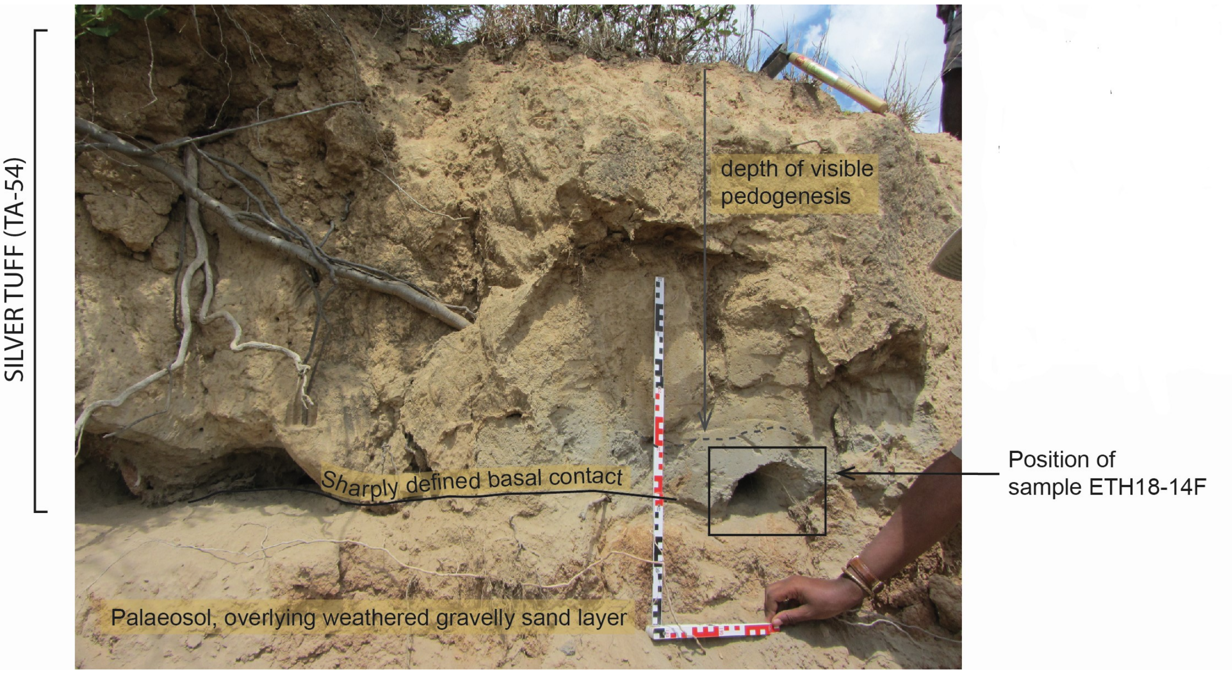

Table S2: WDS-EPMA analyses of CHB_T74.755 and ETH18-14F.

		SiO2	TiO2	Al2O3	FeO	MnO	MgO	CaO	NaO	K2O	P2O5	Cl ppm	Total	
Sample	**#**						**wt %**					**ppm**	**wt %**	*Rundate*
CHB_T74.755	*OxT10662_1*	69.86	0.28	8.98	4.73	0.23	0.01	0.25	5.05	3.85	0.02	1061	93.39	*021116*
	OxT10662_2	69.40	0.28	8.50	4.96	0.22	0.04	0.22	5.10	4.15	0.02	1305	93.05	*021116*
	OxT10662_4	70.14	0.39	9.08	4.82	0.24	0.01	0.25	4.86	4.23	0.00	1142	94.16	*021116*
	OxT10662_9	70.14	0.30	9.03	4.62	0.17	0.01	0.24	4.67	4.18	0.01	1061	93.50	*021116*
	OxT10662_19	69.40	0.28	7.94	6.17	0.30	0.01	0.26	5.31	3.99	0.00	2040	93.91	*021116*
	OxT10662_20	69.40	0.33	8.66	5.18	0.17	0.07	0.24	4.95	3.88	0.04	1142	93.06	*021116*
	OxT10663_1	70.56	0.36	9.15	4.60	0.20	0.02	0.21	4.69	4.28	0.00	1224	94.22	*021116*
	OxT10663_2	70.02	0.27	8.11	5.70	0.24	0.03	0.23	5.87	3.98	0.02	1632	94.67	*021116*
	OxT10663_4	70.59	0.24	9.56	4.22	0.22	0.00	0.20	4.53	4.41	0.03	1142	94.14	*021116*
	OxT10663_5	70.03	0.31	8.58	5.36	0.25	0.00	0.19	5.41	4.02	0.01	1224	94.31	*021116*
	OxT10663_6	69.98	0.34	8.94	5.12	0.14	0.01	0.19	5.02	3.93	0.00	1142	93.81	*021116*
	OxT10663_13	70.54	0.33	9.19	4.65	0.26	0.01	0.21	5.01	4.16	0.02	1142	94.52	*021116*
	OxT10663_18	70.68	0.36	9.07	4.68	0.26	0.00	0.24	5.08	4.33	0.00	1061	94.83	*021116*
	OxT10663_19	68.98	0.27	8.05	5.88	0.35	0.00	0.22	5.39	3.58	0.03	1550	92.94	*021116*
	OxT9984_3	69.02	0.32	8.03	5.99	0.28	0.06	0.25	5.37	3.99	0.03	2045	93.58	*031116*
	OxT9984_4	69.91	0.30	8.98	4.34	0.31	0.00	0.23	4.79	3.94	0.00	1199	92.96	*031116*
	OxT9984_5	70.55	0.35	8.82	5.16	0.18	0.00	0.22	4.87	3.45	0.02	1473	93.80	*031116*
	OxT9984_6	68.95	0.26	7.91	5.88	0.38	0.03	0.19	5.75	3.97	0.01	1922	93.57	*031116*
	OxT9984_7	70.18	0.33	8.95	4.74	0.26	0.00	0.21	4.92	4.33	0.00	1187	94.07	*031116*
	OxT9984_8	70.47	0.34	9.09	4.70	0.19	0.00	0.24	5.13	4.43	0.00	1166	94.74	*031116*
	OxT9984_10	70.06	0.34	8.80	4.56	0.23	0.00	0.23	4.78	4.51	0.02	958	93.65	*031116*
	OxT9984_12	69.18	0.28	8.71	5.17	0.29	0.01	0.24	5.08	3.39	0.00	1231	92.50	*031116*
	OxT9984_13	69.25	0.29	8.09	5.68	0.28	0.00	0.22	5.27	3.97	0.00	1629	93.25	*031116*
	OxT9984_14	70.54	0.34	8.91	4.55	0.21	0.01	0.21	4.77	4.05	0.00	1021	93.72	*031116*
	OxT9984_16	70.30	0.32	8.09	6.14	0.30	0.02	0.24	5.42	4.12	0.01	1838	95.18	*031116*
	OxT9984_18	69.09	0.31	7.97	6.14	0.25	0.02	0.21	5.87	4.36	0.04	1815	94.48	*031116*
	OxT9984_19	70.79	0.36	9.12	4.82	0.18	0.04	0.25	4.67	4.35	0.00	1073	94.70	*031116*
	OxT9984_20	70.54	0.37	9.24	4.39	0.21	0.01	0.26	4.87	4.13	0.00	1227	94.17	*031116*
	OxT9984_21	69.51	0.27	8.00	6.20	0.31	0.00	0.20	5.80	4.16	0.02	1670	94.67	*031116*
	OxT9984_23	69.97	0.33	8.90	5.03	0.26	0.03	0.24	5.05	3.80	0.00	1367	93.78	*031116*
	OxT9984_24	69.70	0.27	7.98	6.16	0.30	0.01	0.19	5.74	4.05	0.00	1866	94.63	*031116*
	OxT9984_25	70.65	0.29	8.91	4.81	0.25	0.05	0.19	4.96	4.36	0.00	1332	94.64	*031116*
	OxT9984_26	69.74	0.35	8.53	5.60	0.26	0.00	0.21	5.20	4.08	0.05	1435	94.19	*031116*
	OxT9984_27	70.38	0.28	8.85	4.47	0.16	0.01	0.23	5.10	3.67	0.00	1083	93.28	*031116*
		SiO_2	TiO_2	Al_2O_3	FeO	MnO	MgO	CaO	Na_2O	K_2O	P_2O_5	Cl	Total	
Sample	**#**						**wt %**					**ppm**	**wt %**	*Rundate*
ETH18-14F (Konso Silver Tuff)	*18-14F_3*	70.00	0.34	8.90	4.97	0.26	0.02	0.22	1.92	4.10	0.01	1380	90.92	*201218*
	18-14F_4	70.79	0.33	9.21	4.75	0.25	0.02	0.21	3.02	4.20	0.00	1084	92.90	*201218*
	18-14F_5	70.95	0.33	9.51	4.40	0.28	0.01	0.23	3.06	4.43	0.00	1128	93.35	*201218*
	18-14F_6	71.10	0.34	9.08	5.24	0.27	0.01	0.22	2.52	4.37	0.03	1465	93.36	*201218*
	18-14F_7	69.55	0.28	8.09	5.75	0.34	0.02	0.23	3.24	4.19	0.02	1905	91.94	*201218*
	18-14F_8	69.98	0.29	8.20	6.08	0.38	0.02	0.23	2.82	4.25	0.02	1840	92.49	*201218*
	18-14F_9	70.86	0.33	9.16	5.22	0.25	0.02	0.21	2.64	4.32	0.03	1465	93.22	*201218*
	18-14F_10	69.56	0.28	8.16	6.05	0.32	0.01	0.22	3.40	4.07	0.02	1910	92.34	*201218*
	18-14F_11	69.62	0.29	8.14	6.01	0.36	0.02	0.26	2.71	4.03	0.02	1935	91.68	*201218*
	18-14F_12	70.15	0.31	8.54	5.79	0.31	0.02	0.21	2.57	4.14	0.01	1912	92.29	*201218*
	18-14F_13	70.03	0.34	9.07	4.55	0.25	0.01	0.23	2.32	4.18	0.00	1318	91.15	*201218*
	18-14F_14	70.92	0.34	8.97	5.25	0.26	0.02	0.24	3.02	4.12	0.00	1388	93.31	*201218*
	18-14F_15	69.30	0.32	8.77	4.95	0.21	0.01	0.22	1.94	4.10	0.00	1467	90.01	*201218*
	18-14F_16	70.55	0.36	8.65	5.05	0.24	0.01	0.21	1.80	4.05	0.01	1361	91.10	*201218*
	18-14F_17	69.22	0.28	8.01	5.90	0.32	0.01	0.20	2.75	3.98	0.01	2328	90.96	*201218*
	18-14F_18	70.12	0.35	8.55	5.21	0.23	0.01	0.22	2.41	4.20	0.02	1327	91.48	*201218*
	18-14F_19	70.00	0.34	8.73	4.91	0.30	0.01	0.24	2.99	4.17	0.00	1513	91.88	*201218*
	18-14F_20	69.63	0.28	8.03	5.82	0.32	0.02	0.22	3.23	4.16	0.01	1826	91.95	*201218*
	18-14F_21	69.71	0.34	8.61	5.09	0.32	0.01	0.24	2.53	4.31	0.03	1508	91.37	*201218*
	18-14F_22	70.83	0.37	10.23	4.20	0.23	0.03	0.29	2.62	4.33	0.02	1076	93.29	*201218*
	18-14F_23	70.17	0.34	8.65	5.02	0.31	0.01	0.23	2.37	4.22	0.00	1376	91.48	*201218*
	18-14F_25	68.68	0.28	7.94	6.06	0.32	0.01	0.23	2.78	4.23	0.03	1861	90.80	*201218*
	18-14F_26	70.88	0.33	8.57	5.46	0.24	0.01	0.22	1.97	4.44	0.03	1405	92.32	*201218*
	18-14F_28	71.12	0.34	8.94	5.17	0.29	0.01	0.24	2.73	4.30	0.02	1394	93.35	*201218*
	18-14F_29	69.73	0.29	8.07	6.03	0.28	0.02	0.20	3.25	4.14	0.02	2004	92.27	*201218*

Table S3: WDS-EMPA secondary standard analyses.

Secondary standard	Runfile	Instrument		SiO2	TiO2	Al2O3	FeO	MnO	MgO	CaO	NaO	K2O	P2O5	ClO	Total
				wt %											
StHs6/80-G	021116-031116	Jeol (Oxford)	n=9	**63.61**	**0.69**	**17.34**	**4.34**	**0.06**	**1.92**	**5.19**	**4.60**	**1.31**	**0.06**	**0.01**	**99.13**
			2σ	*0.67*	*0.10*	*0.69*	*0.35*	*0.08*	*0.14*	*0.17*	*0.22*	*0.11*	*0.09*	*0.02*	
	201218	Cameca	n=4	**63.53**	**0.71**	**17.57**	**4.35**	**0.07**	**1.99**	**5.30**	**4.35**	**1.36**	**0.16**	**0.01**	**99.40**
		(Cambridge)	*2σ*	*0.26*	*0.02*	*0.19*	*0.15*	*0.06*	*0.05*	*0.15*	*0.15*	*0.02*	*0.03*	*0.03*	
		GeoRem preferred value:		***63.70***	***0.70***	***17.80***	***4.37***	***0.08***	***1.97***	***5.28***	***4.44***	***1.29***	***0.16***	***0.03***	
		uncertainty (95%CL)		*0.50*	*0.02*	*0.20*	*0.07*	*0.00*	*0.04*	*0.09*	*0.14*	*0.02*	*0.02*		
Atho-G	021116-031116	Jeol (Oxford)	n=13	**75.12**	**0.24**	**12.14**	**3.21**	**0.13**	**0.10**	**1.69**	**4.13**	**2.76**	**0.01**	**0.03**	**99.56**
			2σ	*0.35*	*0.06*	*0.34*	*0.34*	*0.08*	*0.03*	*0.10*	*0.23*	*0.16*	*0.03*	*0.02*	
	201218	Cameca	n=14	**75.67**	**0.24**	**11.97**	**3.32**	**0.12**	**0.10**	**1.76**	**2.96**	**2.79**	**0.02**	**0.03**	**98.97**
		(Cambridge)	*2σ*	*0.68*	*0.02*	*0.65*	*0.30*	*0.04*	*0.01*	*0.08*	*0.19*	*0.07*	*0.02*	*0.04*	
		GeoRem preferred value:		***75.60***	***0.26***	***12.20***	***3.27***	***0.11***	***0.10***	***1.70***	***3.75***	***2.64***	***0.03***	***0.05***	
		uncertainty (95%CL)		0.70	0.02	0.20	0.10	0.01	0.01	0.03	0.31	0.09	*0.00*		

Supplementary information section S3: Bayesian age-depth model

Input code for Bayesian age-depth model run in OxCcal v4.4.3 (Bronk Ramsey, 2009; 2017):

```
Options()
 {
  Resolution=100;
 };
 Plot()
 {
  Delta_R(U(0,3000));
  P_Sequence("",1,2,U(-2,2))
  {
   Boundary();
      Date("A117-2: 25-30",N(1950.5-628000,12000))
    {
     z=292.118;
    };
Date("A111Q1: 50-63",N(1950.5-561000,14000))
    {
     z=276.725;
    };
      Date("A097-1: 23-52",N(1950.5-428000,7700))
    {
     z=234.480;
    };
Date("B101Q1: 11-120",N(1950.5-438000,37000))
    {
     z=234.067;
    };
     Date("B38E3: 62-76.5; Silver Tuff?",N(1950.5-155000,7000))
    {
     z=74.755;
    };
 Date("B35E1: 17-24",N(1950.5-172000,12000))
```

```
{
 z=68.855;
};
Date("B22H1: 34-42",N(2015.5-81460,5260))
{
 z=47.229;
};
Date("B18H1:51.5-57",N(2015.5-76190,4950))
{
 z=40.726;
};
Date("B16H1:85-90",N(2015.5-84000,6000))
{
 z=38.019;
};
Date("B15H2: 69-76",N(2015.5-61100,4060))
{
 z=36.622;
};
Date("A15A1:65-69",N(2015.5-73360,5080))
{
 z=34.344;
};
Date("A14A2: 42-47",N(2015.5-57430,4060))
{
 z=32.824;
};
Date("B11H1:28-33",N(2015.5-64950,4230))
{
 z=29.761;
};
Date("A11E1: 14-20",N(2015.5-54630,3890))
{
 z=24.373;
};
Date("B9H1:22-33",N(2015.5-47810,3270))
{
 z=23.988;
};
Date("B8H2: 47-58",N(2015.5-48350,2910))
{
 z=22.733;
};
Date("B8H1:22-33",N(2015.5-43950,2550))
{
 z=20.986;
};
Date("B7H2:123-135",N(2015.5-45300,3190))
{
 z=20.458;
};
R_Date("OxA-35657",34164,4427)
{
 z=11.745;
};
Date("B5H1:125-136",N(2015.5-35730,2440))
{
 z=10.86;
};
R_Date("OxA-35913",27501,1897)
{
 z=8.252;
};
R_Date("OxA-35949",12123,238)
{
```

```
   z=6.359;
  };
  R_Date("OxA-35912",10687,182)
  {
   z=4.264;
  };
  Date("A3H1:28-40",N(2015.5-9880,560))
  {
   z=4.251;
  };
  Date("B2E2:15-30",N(2015.5-11760,760))
  {
   z=3.996;
  };
  R_Date("OxA-35974",9933,160)
  {
   z=3.046;
  };
  Date("A2E1: 36.5-54.5",N(2015.5-6530,320))
  {
   z=2.683;
  };
  Date("B1E2:69-79",N(2015.5-5870,290))
  {
   z=2.28;
  };
  R_Date("OxA-35948",4882,75)
  {
   z=1.55;
  };
  Date("B1E1: 45-62",N(2015.5-3150,500))
  {
   z=0.815;
  };
  Boundary(N(2014,1))
  {
   z=0;
  };
 };
};
```

Roberts, H.M., Bronk Ramsey, C., Chapot, M.S., Deino, A.L., Lane, C.S., Vidal, C., Asrat, A., Cohen, A., Foerster, V., Lamb, H.F., Schäbitz, F., Trauth, M.H., Viehberg, F. (2021). Using multiple chronometers to establish a long, directy-dated lacustrine record: constraining >600,000 years of environmental change at Chew Bahir, Ethiopia. (Invited research article). Quaternary Science Reviews. DOI: 10.1016/j.quascirev.2021.107025

Figure S3: Reservoir offset, determined through the Bayesian modelling process described in Section 5.